



**HAL**  
open science

# Dynamics and sources of last glacial aeolian deposition in southwest France derived from dune patterns, grain-size gradients and geochemistry, and reconstruction of efficient wind directions

Luca Sitzia, Pascal Bertran, Adriana Sima, Philippe Chery, Alain Queffelec,  
Denis-Didier Rousseau

## ► To cite this version:

Luca Sitzia, Pascal Bertran, Adriana Sima, Philippe Chery, Alain Queffelec, et al.. Dynamics and sources of last glacial aeolian deposition in southwest France derived from dune patterns, grain-size gradients and geochemistry, and reconstruction of efficient wind directions. *Quaternary Science Reviews*, 2017, 170, pp.250 - 268. 10.1016/j.quascirev.2017.06.029 . hal-01696080

**HAL Id: hal-01696080**

**<https://inrap.hal.science/hal-01696080v1>**

Submitted on 30 Jan 2018

**HAL** is a multi-disciplinary open access archive for the deposit and dissemination of scientific research documents, whether they are published or not. The documents may come from teaching and research institutions in France or abroad, or from public or private research centers.

L'archive ouverte pluridisciplinaire **HAL**, est destinée au dépôt et à la diffusion de documents scientifiques de niveau recherche, publiés ou non, émanant des établissements d'enseignement et de recherche français ou étrangers, des laboratoires publics ou privés.

1 **Dynamics and sources of last glacial aeolian deposition in southwest France derived**  
2 **from dune pattern, grain-size gradients and geochemistry, and reconstruction of**  
3 **efficient wind directions.**

4

5 Luca Sitzia<sup>1</sup>, Pascal Bertran<sup>2,3</sup>, Adriana Sima<sup>4</sup>, Philippe Chery<sup>5</sup>, Alain Queffelec<sup>3</sup>, Denis-  
6 Didier Rousseau<sup>6,7</sup>

7

8 <sup>1</sup> Universidad de Tarapacá, Instituto de Alta Investigación, Laboratorio de Análisis e  
9 Investigaciones Arqueométricas, Antofagasta 1520, 1010069 Arica, Chile

10 <sup>2</sup> INRAP, 140 avenue Leclerc, 33130 Bègles, France

11 <sup>3</sup> PACEA, Université de Bordeaux – CNRS, bâtiment B18, allée Geoffroy-Saint-Hilaire,  
12 33615 Pessac cedex, France

13 <sup>4</sup> Laboratoire de Météorologie Dynamique/IPSL, Sorbonne Universités, UPMC Université  
14 Paris 06, ENS, PSL Research University, École polytechnique, Université Paris Saclay,  
15 CNRS, Paris, France

16 <sup>5</sup> Bordeaux Sciences Agro, 1 cours du Général de Gaulle, CS 40201, 33175 Gradignan,  
17 France

18 <sup>6</sup> Laboratoire de Météorologie Dynamique/IPSL, Département de géosciences, ENS, PSL  
19 Research University, École Polytechnique, Université Paris Saclay, Sorbonne Universités,  
20 UPMC Université Paris 06, CNRS, Paris, France

21 <sup>7</sup> Lamont-Doherty Earth Observatory of Columbia University, Palisades, NY 10964, USA

22

23 **Abstract**

24 Dune pattern, grain-size gradients and geochemistry were used to investigate the sources and  
25 dynamics of aeolian deposition during the last glacial in southwest France. The coversands  
26 form widespread fields of low-amplitude ridges (zibars), whereas Younger Dryas parabolic  
27 dunes mainly concentrate in corridors and along rivers. Spatial modelling of grain-size  
28 gradients combined with geochemical analysis points to a genetic relationship between  
29 coversands and loess, the latter resulting primarily from dust produced by aeolian abrasion of  
30 the coversands. The alluvium of the Garonne river provided also significant amounts of dust  
31 at a more local scale. The geochemical composition of loess shows much lower scattering  
32 than that of coversands, due to stronger homogenisation during transport in the atmosphere.  
33 Overall, sandy loess and loess deposits decrease in thickness away from the coversands. Dune  
34 orientation and grain-size gradients suggest that the efficient winds blew respectively from the

35 W to the NW during the glacial, and the W-SW during the Younger Dryas. A comparison  
36 between the wind directions derived from the proxy data and those provided by  
37 palaeoclimatic simulations suggests a change of the main transport season. Ground surface  
38 conditions and their evolution throughout the year, i.e. the length of the season with snow and  
39 frozen or moist topsoil, and the seasonal distribution of wind speeds able to cause deflation  
40 are thought to have been the main factors that controlled the transport season in the study  
41 area.

42

43 Key words: coversand, loess, Last Glacial, dunes, grain-size modelling, geochemistry, wind  
44 direction, southwest France

45

## 46 1. Introduction

47

48 In the Aquitaine basin (Southwest France), Pleistocene coversands spread over a surface of  
49 approximately 12,000 km<sup>2</sup>, and are bordered on their eastern and southern margins by a large  
50 loess belt. The stratigraphy of aeolian deposits has been the focus of recent studies and a large  
51 set of <sup>14</sup>C, ESR and OSL ages is available both for coversands and loess (Bertran et al., 2009,  
52 2011; Hernandez et al., 2012; Sitzia et al., 2015). Mapping of aeolian deposits has also been  
53 the subject of many attempts. The conventional field approach allowed precise delineation of  
54 the coversands since the 60's (Enjalbert, 1960; Legigan, 1979), but the loess deposits were  
55 always omitted in the maps, and are still lacking on the current 1/50,000 geological map of  
56 France (*infoterre.brgm.fr*). Bertran et al. (2011) showed the potential of coupling field  
57 mapping and the use of soil databases designed for agricultural purposes, in which physico-  
58 chemical analyses of topsoil samples are listed. A first map of loess and transitional facies  
59 was produced using the online BDAT database (*www.gissol.fr*) where the sand, silt and clay  
60 content of topsoil samples are averaged at the scale of administrative units of an area of tens  
61 of square kilometers. Since then, the Land Use and Cover Area frame Statistical survey  
62 (LUCAS) database on topsoil properties in Europe has been made available and was used for  
63 further mapping of aeolian deposits (Bertran et al., 2016). The points which satisfy the grain-  
64 size criteria of coversands and loess were extracted from the rasters of predicted soil texture  
65 established by kriging of the LUCAS data by Balabio et al. (2016). These rasters have a  
66 resolution of 500 m. A comparison with previous maps showed a good fit in most of the  
67 tested areas in Europe (Bertran et al., 2016). Improvement of the French database (Donesol,

68 <http://acklins.orleans.inra.fr/outil/donesol>) and access to raw data makes it now possible to  
69 investigate more in detail the aeolian deposits at a regional scale, since more refined  
70 information on grain-size composition and on loess thickness is available.

71

72 Pioneer mineralogical studies have been performed by Klingebiel (1966) and Legigan (1979).  
73 They have suggested that the sources of the coversands were mostly Mio-Pliocene alluvial  
74 and deltaic sands that crop out on the continental plateau. However, these studies remain  
75 crude, and the possible contribution of wind-blown particles derived from the alluvium fed by  
76 the surrounding ranges (Massif Central, Pyrenees) was hardly detectable using heavy mineral  
77 analyses alone. The provenance of the particles and the transport paths remain, therefore, to  
78 be documented in detail. Grain-size gradients (Lautridou, 1985; Ruegg, 1983; Liu, 1988),  
79 loess thickness (Frazee et al., 1970; Mason, 2001), and the mineralogical and chemical  
80 composition of the deposits (Muhs et al., 2008; Stevens et al., 2010; Rousseau et al. 2014)  
81 have proved to be efficient tools for reconstructing the transport paths at a regional scale and  
82 for identifying the main factors involved in deposition. Together with dune orientation, these  
83 data give insight into past atmospheric circulation and have been widely used for  
84 reconstructing wind directions during the Last Glacial in Europe (Poser, 1950; Maarleveld,  
85 1960; Léger, 1990; Isarin et al., 1997; Zeeberg, 1998; Van Huissteden et al., 2001; Renssen et  
86 al., 2007).

87

88 The aim of this paper is to combined geomorphological, sedimentological and geochemical  
89 approaches to better understand the origin and dynamics of the aeolian deposition in  
90 southwest France. Then, the reconstructed wind regimes during the Last Glacial in the study  
91 area are compared with previous climatic simulations (Sima et al., 2009, 2013), in an attempt  
92 to identify the period of the year favourable to dust activity for different climate patterns.

93

## 94 **2. Geological setting**

95

96 Since the beginning of the Middle Pleistocene, the centre of the Aquitaine basin was quite  
97 similar to its current configuration and corresponded to a sand plain almost lacking relief and  
98 gently sloping toward the Atlantic Ocean. Such a context, unparalleled along the French  
99 coast, favoured the accumulation and preservation of aeolian deposits throughout the glacial  
100 phases of the Pleistocene (Bertran et al., 2011; Sitzia et al., 2015).

101

102 At the basin scale, the following geomorphological units have been distinguished (Fig.1B) :  
103 (1) ventifact pavements, present mainly in the northern part of the basin at the surface of the  
104 plateau alluvium on both sides of the Garonne River (Plateau Girondin and Blayais) ; (2) the  
105 coversands (“Sable des Landes Formation” *sensu* Sitzia et al., 2015), limited by the Garonne  
106 river to the east and the north, the Adour river to the south, and the Atlantic Ocean to the  
107 west; (3) a large loess belt mainly developed to the east and the south of the coversands.

108  
109 Recent works allowed reappraisal of the regional chronostratigraphy of sand and loess  
110 deposits (Bertran *et al.*, 2009, 2011; Sitzia et al., 2015). Three main phases of coversand  
111 accumulation were identified throughout the Last Glacial (Sitzia et al. 2015): (1) Marine  
112 Isotopic Stage (MIS) 4-3 (64-32 ka), characterized by predominant wet sandsheet  
113 accumulation; (2) MIS 2 and the beginning of MIS 1 (Greenland Interstadial 1e) (25-14 ka),  
114 associated with the development of dry sandsheets and coincident with the maximum  
115 expansion of the Landes desert; (3) Younger Dryas (YD, Greenland Stadial 1), marked by the  
116 development of parabolic dune fields. Parabolic and dome dunes dating back to the 14<sup>th</sup>-19<sup>th</sup>  
117 centuries have also been documented and probably reflect local dune reactivation due to  
118 increased human impact on the vegetal cover during the Little Ice Age (Bertran et al., 2011).

119  
120 Sitzia et al. (2015), through the analysis of the chronological data of near-surface coversands,  
121 revealed an uneven geographical distribution of the ages. They are dominantly Middle  
122 Pleistocene in the northernmost part, MIS 4-3 in the Plateau Girondin, and MIS 2 to YD in the  
123 Plateau Landais to the south. According to the authors, this pattern might have resulted from a  
124 deficit in sand in the north during the Last Glacial Maximum (LGM) since the emerged  
125 continental plateau was much wider (and as a consequence, the coastline was more distant)  
126 than in the south. Available ages for loess suggest that they accumulated mainly during the  
127 two last glacial periods (Bertran et al., 2011; Hernandez et al., 2012).

128

### 129 **3. Modern wind regime.**

130

131 Prevailing winds along the Atlantic coast of mid-latitude Western Europe are handled by two  
132 major pressure areas, the Azores High, located in the Atlantic Ocean between latitude 25 and  
133 40°N, and the Icelandic Low, located between latitude 60 and 75°N. Seasonally, the position  
134 of these two pressure centres shifts and the wind regime changes. During the winter, dominant  
135 winds come from the southeast, whereas westerly to northwesterly winds are the most

136 prominent during the summer (Fig. 2A). The map of mean wind speeds at 10 m available at  
137 the European Joint Research Centre (<http://agri4cast.jrc.ec.europa.eu/DataPortal>) shows the  
138 following (Fig.2B):

139

140 (1) The highest wind speeds are observed along the coast and in the Garonne estuary  
141 where channelling of the airflows leads to wind acceleration;

142

143 (2) Overall, the wind speeds decrease the further the altitude increases;

144

145 (3) The area with the lowest mean wind speed is located at the southern edge of the  
146 Pleistocene coversands.

147

#### 148 **4. Data and methods**

149

##### 150 *4.1. Analysis of dune patterns*

151

152 The pattern of the dune ridges has been analysed using (1) digitized black-and-white aerial  
153 photographs from the 1950 missions (1/25,000) of the French Institut Géographique National  
154 (IGN) and (2) IGN aerial colour photographs available on Google Earth. The main dune  
155 morphologies were described according to McKee (1979). To establish the crest direction we  
156 followed the approach proposed by Ewing et al. (2006). For barchanoid ridges, a line parallel  
157 to the general direction of the dune crest was used.

158

159 Most of the parabolic dunes have been mapped during the 1/50,000 geological survey of the  
160 Aquitaine basin by the French Bureau des Recherches Géologiques et Minières (BRGM)  
161 (Capdeville and Dubreuilh, 1994). The dune morphologies were described according to the  
162 terminology of Pye and Tsoar (2009), and the growth direction was measured using the  
163 bisector of the angle between the two arms of the dune.

164

165 Where available, the Digital Elevation Model (DEM) 5 m of the IGN (RGE Alti® 2.0, ©IGN  
166 2014) made it possible the observation of the detailed morphology of the parabolic dunes.  
167 Since the small aeolian ridges remain difficult to identify from the DEM, a photogrammetric  
168 survey has been performed with a drone in 3 areas of 1 to 8 km<sup>2</sup>, which provided more precise  
169 elevation data. The pixel resolution is 0.3 m.

170

171 *4.2. Grain size, thickness and geochemistry of the aeolian deposits*

172

173 The grain size and thickness dataset consists of (1) data collected in this work or previously  
174 published (Bertran et al., 2009, 2011; Dubreuilh, 1976; Thibault, 1970), and (2) data available  
175 from the Donesol database (INRA, 2011) for the Gironde, Landes, Dordogne and Lot-et-  
176 Garonne districts. The datasets were cleaned to select only the outcrops and the stratigraphical  
177 units of aeolian origin. The selected data were finally treated for the purpose of geostatistical  
178 analysis.

179

180 The samples for grain-size analysis were processed in the PACEA laboratory (Université de  
181 Bordeaux) using a Horiba LA-950 laser particle size analyser. The sample pre-treatment  
182 includes suspension in sodium hexametaphosphate (5 g/L) and hydrogen peroxide (35%) for  
183 12 hours, and 60 seconds of ultrasonification in the analyser to achieve optimal dispersion.  
184 The Mie solution to Maxwell's equations provided the basis for calculating the particle size as  
185 is recommended by the ISO committee (Jones, 2003; ISO, 2009), using a refractive index of  
186 1,333 for water and 1.55i - 0.01i for the particles (see Supplementary Information 2). In the  
187 Donesol database, the grain-size limits are those used by the French pedologists (Duchaufour,  
188 1997), i.e. 2000–200  $\mu\text{m}$  (coarse sand), 200–50  $\mu\text{m}$  (fine sand); 50–20  $\mu\text{m}$  (coarse silt); 20–2  
189  $\mu\text{m}$  (fine silt); <2  $\mu\text{m}$  (clay). The analyses used in the database have been done by wet sieving  
190 of the particles >50  $\mu\text{m}$  and with the pipette method for the particles <50  $\mu\text{m}$ . The results  
191 obtained with this method cannot be directly compared with those obtained with the laser  
192 particle size analyser (Konert and Vandenberghe, 1997; Buurman et al., 2001; Antoine et al.,  
193 2001). Here, after comparing 20 samples treated using both methods, the following limit  
194 classes have been chosen: <4.6  $\mu\text{m}$  (clays), 4.6–26  $\mu\text{m}$  (fine silt), 26–50  $\mu\text{m}$  (coarse silt),  
195 >50  $\mu\text{m}$  (sand). These limits are similar to those used by Antoine et al. (2003). Polymodal  
196 grain size distributions expressed in phi units have been deconvoluted in populations of  
197 particles characterized by a Gaussian distribution using the software Fityk 0.9.8 (Wojdyr,  
198 2010) to identify precisely the main modes and to follow their spatial evolution.

199

200 The samples selected for the geochemical analysis (n=77) come from outcrops studied during  
201 this work or previously published (Bertran et al., 2009, 2011; Sitzia et al. 2015). The outcrops  
202 have been selected in order to characterize the main types of aeolian deposits and their  
203 potential sources: (1) Last Glacial coversands n=22) ; (2) YD parabolic dunes (n=13) ; (3)

204 loess from the Landes area (n=17) ; (4) loess from the Entre-Deux-Mers area (n=4) ; (5)  
205 recent alluvium of the Leyre (n=4), the Ciron (n=3), the Garonne (n=3) and the Adour (n=3)  
206 rivers; (6) Plio-Pleistocene plateau alluvial deposits (n=7). The samples from aeolian sands  
207 have been taken below the B horizon of the surface podzol. All the loess samples come from  
208 the argillic Bt horizon and were taken between 0.6 and 0.9 m deep. After removing the grains  
209 >2 mm, the sand fraction was separated from the component <63  $\mu\text{m}$  by wet sieving and  
210 crushed. The sand and the fine fractions have been analyzed apart by Energy Dispersive X-  
211 Ray Fluorescence (ED-XRF) by the spectrometry division of Ametek (Elancourt, France).  
212 The measurements were made with a XEPOS instrument and do not allow quantification of  
213 elements lighter than aluminum. Quantification was based on fundamental parameters.

214

215 Some representative samples of aeolian deposits and possible sources have been studied by X-  
216 Ray Diffraction (XRD). As for ED-XRF, the sand and silt/clay fractions were studied  
217 separately. The analysis was carried out by the Institut de Chimie de la Matière Condensée in  
218 Bordeaux (ICMCB) using a PANalytical X'Pert diffractometer with a Bragg - Brentano theta  
219 – theta configuration. The measurements were made with a measuring time of 30 mn,  
220 between 8 and 80° and with a minimum step angle of 0.02°. Mineralogical identification was  
221 performed using the EVA software coupled with a JCPDS-ICDD PDF2 database.

222

223 The grain-size and the geochemical data are expressed as percentages; therefore, they have to  
224 be considered as compositional data (Aitchison, 1982). The analysis of compositional data by  
225 classic multivariate statistics provides inappropriate results (Aitchison, 1982). Aitchison  
226 (1986) proposed a robust solution to this problem, which used the logarithms of component  
227 ratios instead of the raw percentages. In this work, because of the nature of the data, we used  
228 non parametric replacement of the null values according to the method proposed by Martín-  
229 Fernández et al. (2003) for below-detection values. Here, all the compositional data were  
230 analysed using the CoDaPack software (Comas and Thió-Henestrosa, 2011).

231

232 For the purpose of geostatistical data analysis, a variographic analysis (Webster and Oliver,  
233 2007) has been carried out with the VarioWin software (Pannatier, 1996). For compositional  
234 data, in agreement with Pawlowsky and Burger (1992), each variable was transformed before  
235 variographic analysis. Here, the Isometric Logratio Transformation has been applied  
236 (Egozcue et al., 2003). Finally, we used ordinary kriging (Webster and Oliver, 2007) for the  
237 interpolation through the geostatistical toolbox of ArcGis 9.3.



238

239 The models obtained have been tested by a double cross validation. In ArcGis, the value of a  
240 variable is estimated in each point of the space by kriging and this operation is repeated every  
241 time by removing one of the points for which the true value was originally known. Following  
242 this procedure, the software calculates the mean error (ME) and the mean square deviation  
243 ratio (MSDR). The mean error has to be close to 0, while the mean squared deviation ratio has  
244 be as close as possible to 1 (Webster and Oliver, 2007). The model validity has been also  
245 measured through an independent data set. The original database (grain size, thickness)  
246 selected for the geostatistical analysis has been split before the variographic analysis using the  
247 random selection spatial tool of ArcGis. We chose to randomly select 10% of the total number  
248 of samples. The remaining 90% have then been used for the variographic analysis and the  
249 calculation of the ME and MSDR statistics. Doing so, it was possible to plot the observed  
250 values (independent data set) against the estimated values and to calculate a linear regression  
251 between the two sets. Following Pawlowsky-Glahn and Olea (2004), the fitness of the  
252 regression for grain-size data was evaluated by calculating the standardized residual sum of  
253 squares (STRESS). The closer the value of the STRESS index to zero, the less is the  
254 difference between observed and estimated values, and thus the best is the tested modeling.

255

#### 256 *4.3. High-resolution glacial climate simulations*

257

258 We dispose of two numerical palaeoclimatic simulations at high-resolution over the studied  
259 area that we can compare to our proxy data. The first simulation, designed for the Last Glacial  
260 Maximum (LGM), was used by Banks et al. (2009) for niche modelling. In this simulation,  
261 the orbital parameters and the atmospheric CO<sub>2</sub> concentration (Berger, 1978; Raynaud et al.,  
262 1993) were set to their values for 21 ka. The LGM ice-sheet configuration (height and extent)  
263 reconstructed by Peltier (2004, ICE-5G) was prescribed, and the land-sea mask was adjusted  
264 to a sea-level drop of about 120 m. The GLAMAP2000 reconstruction of the LGM sea-  
265 surface temperatures (SSTs) and sea-ice extent was imposed (Paul and Schäfer-Neth, 2003;  
266 Sarnthein et al., 2003). The second simulation is one of the numerical experiments used by  
267 Sima et al. (2009, 2013) to study the European climate (and dust) sensitivity to changes in  
268 North-Atlantic SSTs as those associated with the MIS 3 millennial-timescale variability. The  
269 orbital parameters and CO<sub>2</sub> concentration are set to 39 ka values, the ice-sheet configuration,  
270 also selected from the ICE-5G reconstructions, corresponds to a sea level about 60 m lower  
271 than today (i.e. half of the LGM value), and the land-sea mask is adapted to the sea-level

272 drop. Because no reconstruction or modelling result was available at that time for MIS 3 sea-  
273 surface conditions, the GLAMAP2000 dataset was imposed in the base-line MIS 3  
274 simulation. A cold and a warm perturbation were obtained by applying zonal anomalies of up  
275 to 2°C to the GLAMAP North-Atlantic SSTs in the latitudinal band between 30°N and 63°N.  
276 Considering the differences of North-Atlantic SSTs between the LGM and an average MIS 3  
277 state suggested by experiments with an earth system model of intermediate complexity (Van  
278 Meerbeeck et al., 2009), here we use the warm perturbation (hereafter “MIS 3” simulation) to  
279 characterize the average MIS 3 conditions in the comparison with the LGM.

280

281 In both MIS 3 and LGM experiments, the modern vegetation cover was prescribed in most  
282 regions, following the PMIP recommendations (e.g. Braconnot, 2004). Thus, in the area of  
283 interest here, trees occupy 60-80% of every grid-point in the coversands (in yellow on Fig.  
284 1B), and about 15- 40% elsewhere. The soil is bare all year long on 5-15% of the grid-points’  
285 surface, and the rest up to 100% of each grid-point is occupied by grass. This is a drawback  
286 because the LGM vegetation was much scarcer. The use of modern vegetation does not affect  
287 the simulated wind direction, but only the wind speed, which is strongly reduced due to  
288 overestimating the roughness length. As the wind speed is a key element in determining the  
289 season(s) when dust emissions occur, we also present sensitivity tests of this variable to more  
290 appropriate values of roughness length. Using prescribed present-day vegetation also leads to  
291 unrealistically overestimating its effect of protecting the ground from aeolian erosion. Thus,  
292 for the impact of the surface conditions on the dusty season, we will only be able to discuss  
293 soil moisture and snow cover.

294

295 The simulations were performed with the LMDZ atmospheric general circulation model  
296 (version 3.3), coupled with the SECHIBA land surface model (Krinner et al., 2005), on a  
297 stretched grid with resolution down to 60 km on Western Europe. For each simulation there  
298 are 21 years of run, one year of spin-up followed by 20 years for analyses.

299

## 300 **5. Results**

301

### 302 *5.1. Dunes*

303

#### 304 5.1.1. Low amplitude dunes

305

306 Among the low amplitude dunes, four main morphological types have been identified from  
307 aerial photographs: transverse ridges, barchanoid ridges, isolated barchanoid ridges and dome  
308 dunes/sand patches. The ridges appear in cultivated areas as bright lineaments separated by  
309 darker interdune areas due to variations in soil organic and water content. Most of the ridge  
310 fields were observed in the Plateau Girondin area, where the groundwater table is close to the  
311 ground surface and the YD parabolic dunes are scarce. According to available chronological  
312 data, these ridges date back to MIS 4-3, or possibly to older phases of sand deposition in the  
313 northernmost area. The DEM provided by photogrammetry shows that the ridge pattern  
314 corresponds to regular to irregular low amplitude reliefs, 0.3 to 0.7 m high and 70 to 150 m in  
315 wavelength (Fig. 3). The reliefs are aligned along the bright lineaments visible in aerial  
316 photographs. In contrast, no significant ridge areas were found in aerial photographs to the  
317 south on the Plateau Landais where the MIS 2 coversands are thicker. Field survey, however,  
318 showed that ridges also were present there in small areas forming well-preserved linear reliefs  
319 approximately 1 m in height (Fig. 4). In cross-sections, all these dune-like forms are  
320 associated to a sandsheet facies; high-angle stratification is almost absent (Sitzia et al., 2015).

321

322 In the Plateau Girondin, the following observations can be made (Fig. 5): (1) the different  
323 types of ridge morphologies form homogeneous fields elongated parallel to the coast; (2) the  
324 dome dunes/sand patches are located on the margins of the barchanoid and transverse ridge  
325 fields; (3) the dune fields are replaced toward the east by an area characterized by thin  
326 sandsheet deposits almost lacking dune-like forms; (4) the distribution of the different types  
327 of morphologies seems to be mainly controlled by topography.

328

329 A total of 425 measurements of crest direction have been made from barchanoid and  
330 transverse ridges. The rose diagrams show that predominant crest directions are consistently  
331 N-S (i.e. the vector perpendicular to dune crests is W-E, Fig. 5A). Local departure from this  
332 direction was found to be mainly controlled by topography. This is particularly obvious in  
333 Figure 5C for the transverse ridges whose crest direction, roughly parallel to the contour lines,  
334 vary between N-S and NE-SW within a few kilometres.

335

### 336 5.1.2. Parabolic dunes

337

338 The parabolic dunes are 10 to 15 m high and exceptionally exceed 25 m (Dune de Cazalis,  
339 Legigan, 1979). The total number of digitized dunes is 2636. Following the typology

340 proposed by Pye and Tsoar (2009), simple (hairpin, lunate), complex (hemicyclic, digitated,  
341 nested, rake-like, en-echelon) and compound (long-walled ridge with secondary transverse  
342 arms) forms were observed.

343

344 The parabolic dunes exhibit a non-random distribution over the landscape. They are mainly  
345 clustered around the rivers, and form corridors up to 80 km in length along shallow valleys  
346 oriented W-E and over the plateau (Fig. 6). The dune morphology changes according to  
347 topography. Along the Leyre and the Ciron valleys, as well as near the coast, the parabolic  
348 dunes are mostly simple; on the contrary, complex and compound forms are mainly observed  
349 in the corridors (Fig. 7A, C). Complex forms several kilometres in length have been observed  
350 in the main dune corridor (Fig. 7B).

351

352 A total of 394 measurements of dune orientation have been made. The rose diagrams reveal a  
353 systematic orientation towards the ENE and a low dispersion of the values (Fig. 6).

354

## 355 *5.2. Grain-size gradients at the basin scale*

356

357 In the Donesol grain-size database, 513 out of the 3683 sites, considered to be pure (i.e. non  
358 colluviated) aeolian deposits, were retained (Fig. 8). Among the selected sites, 462 were used  
359 in the geostatistical analysis and 51 for cross-validation. The results of cross-validation (see  
360 Supplementary Information) indicate that both the variographic analysis and the ordinary  
361 kriging were satisfactory. The interpolated maps of the content in coarse sand, fine sand,  
362 coarse silt and fine silt are shown in Figure 8. The following observations can be made: (1)  
363 every grain-size class shows a gradient oriented NW-SE; (2) the coarse fractions are mainly  
364 located in the north-western part of the basin and extend inland from Arcachon to the SE; (3)  
365 the Garonne and Adour valleys (and their tributaries) serve as limits for the coversands; the  
366 silty sand facies are restricted to a narrow strip on the left bank of the Garonne river, whereas  
367 they form a broader band on the right bank and in the southern part of the basin; (4) in the  
368 loess belt, the ratio coarse/fine silt varies only slightly in the study area. When increasing the  
369 number of grain-size classes, it can be observed that, both in the Entre-Deux-Mers area and in  
370 the southern part of the basin, the coarse silt maximum is located northwest of the fine silt  
371 maximum (Fig. 9). Comparison between these maps and that derived from the LUCAS  
372 database (Fig. 1) shows that loess have a more limited extent in the latter, where the mapped  
373 aeolian units have, therefore, to be considered as minimal.

374

375 The sand deposits extend up to the border of the Landes plateau and show a main mode  
376 ranging between 340  $\mu\text{m}$  for the northernmost site (Retjons) and 270  $\mu\text{m}$  for the southernmost  
377 one (Pujo-le-Plan) (Fig. 10B). In the Adour valley and its tributaries, the distribution is  
378 polymodal. From the north to the south, the main mode is first in medium sands (270  $\mu\text{m}$ ) and  
379 then decreases rapidly and gives way to a mode on silts (22  $\mu\text{m}$ ). In this area it can be noticed  
380 (1) a rapid decrease in the size of the sand particles (Fig. 10B); (2) a decrease in the  
381 contribution of the coarse modes in favour of the finer modes (Fig. 10C). Finally, south to the  
382 Adour valley, a mode around 17  $\mu\text{m}$  becomes predominant (Fig. 11A). This mode decreases  
383 from 17 to 14  $\mu\text{m}$  quite evenly as a function of the distance to the coversands. For all the sites  
384 located between the Adour valley and the Pyrenean foothills, significant amounts of clay are  
385 present. The mode, close to 3  $\mu\text{m}$ , remains steady regardless of the distance to the coversands  
386 (Fig. 11A), whereas the total clay content slowly increases with distance (Fig. 10D).

387

388 In the northern part of the basin, the grain-size distributions show that (1) the sands of the  
389 Blayais area are relatively coarse (mode between 300 and 600  $\mu\text{m}$ ); (2) the silts of the Entre-  
390 Deux-Mers area have a mode between 30 and 34  $\mu\text{m}$ ; this is appreciably coarser than the  
391 mode of the loess deposits in the southern part of the basin; (3) the silt mode decreases  
392 significantly toward the SE. The most distant sample from the sources (Barbas) has a mode  
393 around 12  $\mu\text{m}$ .

394

### 395 *5.3 Thickness variability at the basin scale*

396

397 According to Karnay et al. (2010), the coversands (Sable des Landes Formation) form a thin  
398 sheet, usually less than 2-3 m thick. Nevertheless, the underlying Castet Formation (Dubreuilh  
399 et al., 1995), which is now considered to be part of the Sable des Landes Formation (Sitzia et  
400 al., 2015) and reaches locally up to 40 m in thickness, was not considered by Karnay et al.  
401 (2010). As a whole, the coversand thickness decreases from the west to the east according to  
402 the distance to the coast and with altitude.

403

404 The loess data were partitioned in two sets, one for the north (n= 292), and the other for the  
405 south (n=434). The geostatistical analysis points out that (1) the ordinary kriging decreases  
406 systematically the standard deviation of the thickness around the mean; (2) the deviation  
407 between measured and estimated values is larger for the northern data set. The Anderson-

408 Darling test reveals that the deviation distribution fits a normal (Gaussian) distribution. For  
409 the southern loess, the accuracy of thickness estimation is 57.4 cm and the mean error is 81.8  
410 cm. The most significant errors are due to extreme values. For the northern loess, the accuracy  
411 of estimation and the mean error cannot be evaluated because the deviation distribution does  
412 not follow a Gaussian function.

413

414 The interpolated maps show that the loess thickness decreases rapidly with increasing  
415 distance to the coversands, in a gradual way in the southern area, more steeply in the northern  
416 area (Fig. 12). The maximum loess thickness reaches 3.5 m in the south and 5 m in the north.  
417 Because of the uneven distribution of the selected Donesol data and the loose geographical  
418 coverage, the interpolated maps do not make it possible to identify if deposition preferentially  
419 occurred on particular slopes according to their orientation.

420

#### 421 *5.4. Geochemistry and potential sources*

422

423 The distribution maps of elemental compositions (Fig. 13) and the scattergrams of the  
424 elements versus Si (Fig. 14) (mainly as quartz) point out the following:

425

426 (1) Zr, the principal component of zircon, and Ti, probably as oxides, are mainly concentrated  
427 in the fine fraction (silt, fine sand). Therefore, these elements are mostly abundant in loess  
428 and in the fine fraction of the coversands. In a Si-Ti diagram, the samples of aeolian deposits  
429 are aligned along a line with a negative slope (Fig. 14, line a), except for the fine fraction of  
430 some coversand samples. This strongly suggests that the most of the aeolian samples result  
431 from the size fractionation of a common source of intermediate composition between that of  
432 sand and that of fines (Fralick and Kronberg, 1997). The samples from the Adour and  
433 Garonne rivers also show a linear trend (line b), but plot on a different line from that of the  
434 aeolian deposits, which indicates different sources. On the contrary, the samples from the  
435 Leyre and the Ciron rivers, which drain both the coversands and old alluvial deposits, plot  
436 among the aeolian samples or between the Adour-Garonne and loess samples. Zr has a  
437 behaviour roughly similar to Ti. The loess composition appears to be homogeneous when  
438 compared with the whole data set. Such an observation is also valid for all the elements.

439

440 (2) Ca, as a component of carbonate or silicate minerals (feldspar, amphibole), is lacking in  
441 the aeolian sand fraction, whereas it has been found in small amount in the alluvial deposits.  
442 Ca has been detected as traces in the fine fraction of a few coversand samples where it is  
443 probably associated with Al in silicate minerals.

444

445 (3) K is present both in the aeolian sand fraction as part of silicate minerals (feldspar,  
446 muscovite) and in slightly larger amounts in the fine fraction (illite, mixed-layer illitic clay).  
447 Mean concentrations are significantly greater in the alluvial deposits. In the Si-K diagram, the  
448 K content of the aeolian sand fraction appears to be uncorrelated to Si and the samples are  
449 aligned on a horizontal line. On average, the sand fraction of loess is depleted in K in  
450 comparison with the coversands. The samples of fine fraction do not plot on the same line as  
451 the sands, but below it, suggesting a loss of K due to alteration and soil leaching (Fralick and  
452 Kronberg, 1997).

453

454 (4) On the Si-Al diagram (Fig. 14), the alignment of the aeolian samples along the same line  
455 suggests a partition of Al between sand and fines due to sedimentary sorting, with Al mainly  
456 concentrated in clays. High Al contents plotting above this line have been found only in the  
457 fine fraction of the coversands. Such enrichment in Al can be related to organic-mineral  
458 complexes in the B horizon of the surface podzol (Righi and De Coninck, 1974; Melkerud et  
459 al., 2000).

460

461 The principal component analysis (“compositional biplot”, Aitchison and Greenacre, 2002)  
462 for the sand fraction (Fig. 15) explains 72.3% of the total variance. The first axis  
463 discriminates the group Ca+K+Rb+Sr from the group Fe+Ti+Zr. K and Rb are mainly related  
464 to K-silicates, mostly feldspar and micas (De Vos et al., 2006; Wedepohl, 1978). Sr has a size  
465 intermediate between K and Ca and can replace these two elements both in silicates and in  
466 carbonate minerals (De Vos *et al.*, 2006). Because of the lack of carbonates in the studied  
467 samples, the group K+Rb+Sr reflects the pole of potassium silicates, while Ca corresponds to  
468 calcium silicates. Fe (+ Cr as a substitute) is present in silicate minerals and in oxides and  
469 hydroxides (De Vos *et al.*, 2006). The group Fe, Ti and Zr thus represents the pole of oxides  
470 and the minerals resistant to alteration.

471

472 The position of the samples in the biplot allows making the following remarks: (1) the  
473 samples of aeolian sands (Landes, Blayais, parabolic\_dunes), the old alluvial terraces of the

474 Garonne river (Plateau\_alluvium), the recent alluvial deposits (Fz) of the Midou and Leyre  
475 rivers (which essentially drain the Sable des Landes Formation) are distributed between the  
476 barycentre of the biplot and the pole quartz + K-silicates; (2) the sand fraction of the southern  
477 loess (Loess\_Landes) is associated with the pole of resistant minerals and oxides; (3) the  
478 recent alluvial deposits (Fz) of the Adour and Garonne rivers, which drain the Pyrenees, plot  
479 apart from the other samples, and are opposed to the pole quartz + resistant minerals; they  
480 include a high proportion of easily alterable Ca-minerals; (4) the sand fraction of the loess  
481 from the Entre-Deux-Mers area is located between the southern loess and the recent alluvial  
482 deposits.

483

484 The biplot for the fine fraction (Fig. 16), which takes into account a larger set of elements  
485 because of values above the detection limit, produces results substantially different from those  
486 for the sand fraction. It explains 63.7% of the total variance. Several poles can be  
487 distinguished. The first correspond to calcium-rich minerals (Ca); the second to resistant  
488 minerals, quartz and zircon (Si+Zr+Hf); the third to potassium silicates (K+Rb, and Ba,  
489 strongly adsorbed by soil clays, Reimann et al., 2014); and finally, the poles of Fe-oxides  
490 (Fe+Cr+As) and of Al-complexes (Al).

491

492 In this biplot, the loess samples appear more homogeneous and plot in the proximity of the  
493 pole oxides and K-silicates (probably dominated by clays). The loess composition partially  
494 covers that of coversands and is located apart of the recent alluvial deposits, which are close  
495 to the pole of Ca-minerals.

496

### 497 *5.5. Results of climate simulations*

498

499 Figure 17 shows the results of the LGM and MIS 3 simulations for wind direction and for the  
500 variables that constrain the period of the year when dust emissions can occur, i.e. daily  
501 maximum wind speed (more informative for dust mobilization than daily average), snow-free  
502 surface fraction, and dry soil depth. The annual cycle of these variables is constructed on daily  
503 data for winds, and on monthly data for surface conditions, averaged over 20 years of run for  
504 each climate state and over the domain between longitude 2°W-1°E and latitude 43°-45.5°N  
505 (delimited by the black rectangle in Fig. 1A and zoomed in Fig. 1B).

506



507 The annual cycle of wind direction (Fig. 17A, B) is similar in the two simulations and not  
508 much different from the present-day one (Fig. 2). In both cases, the winds blow from W-SW  
509 in winter, turn from W in springtime, then from W-NW in summer. A reverse evolution  
510 occurs from the summer to the winter, through westerly winds in autumn. The daily  
511 maximum wind speed, averaged over the domain and over 20 years of run (black curves in  
512 Fig. 17C, D), is highest in winter, lowest in summer, and springtime values are higher than  
513 autumn ones. The LGM daily maximum winds are generally stronger than for MIS 3,  
514 especially from mid-May to October. The differences are small, and the values themselves are  
515 relatively low, less than  $7 \text{ m.s}^{-1}$ . When looking at individual grid cells and individual days of  
516 the 7200-point time series (i.e., 20 years x 360 days/year of run on a 360-day calendar), the  
517 highest (winter) daily maximum winds in the MIS 3 run often exceed  $12 \text{ m.s}^{-1}$ , with peaks at  
518 about  $16 \text{ m.s}^{-1}$ , while in the LGM simulation the winter values are frequently above  $16 \text{ m.s}^{-1}$ ,  
519 with extremes above  $20 \text{ m.s}^{-1}$ . The simulated winds are thus too weak considering the strong  
520 dust activity suggested by the field data. This is due to the high values of the roughness length  
521 ( $z_0$ ) calculated by the model on the basis of the present-day vegetation cover that was  
522 prescribed in both simulations. For comparison,  $z_0$  is about 37 cm on average on the studied  
523 domain, while values of 1 cm are associated in the model to bare soil. The vegetation was  
524 considerably scarcer than today for both LGM and average MIS 3 climates, so we recalculate  
525 and plot the daily maximum winds for two values of  $z_0$  more adapted to the investigated area  
526 and periods. The blue curves in Fig. 17C, D correspond to  $z_0 = 1.5 \text{ cm}$ , and the green ones to  
527  $z_0 = 4 \text{ cm}$ . The first  $z_0$  value is the one that the model would calculate for a surface covered  
528 by about 50% of grass, and the rest of bare soil. The second one corresponds to a majority of  
529 grass, with less than 10% bare soil and less than 10% trees (that can be assimilated to shrubs,  
530 which are not represented in the model). With these lower  $z_0$ , the averages of daily maximum  
531 wind increase considerably, they almost double for  $z_0 = 1.5 \text{ cm}$ . Looking at individual days  
532 and grid cells, even for the relatively less windy MIS 3 and the lower test value  $z_0 = 4 \text{ cm}$ , the  
533 maximum daily values regularly exceed  $25 \text{ m.s}^{-1}$  in winter, with a few peaks around  $40 \text{ m.s}^{-1}$ .  
534

535 Park and In (2003) have statistically determined a wind-speed threshold of  $7.5 \text{ m.s}^{-1}$  for dust  
536 mobilization in sandy areas from Asian deserts. If we consider this limit to also apply to the  
537 Landes coversands, the LGM average maximum winds practically never drop below it in the  
538 test with  $z_0=1.5 \text{ cm}$ , so that only the surface conditions would determine the dusty part of the  
539 year. For the MIS 3 run, the average daily maximum winds drop below the threshold in July  
540 for  $z_0 = 1.5 \text{ cm}$ , at mid-May for  $z_0 = 4 \text{ cm}$  respectively, and strengthen again in November in

541 both tests. The tests with these  $z_0$  values can be interpreted in two ways. When comparing  
542 LGM to MIS 3, using the spatial averages of variables over the entire domain, the blue curve  
543 for the lower  $z_0$  (for about 50% grass and 50% bare soil) is more appropriate to characterize  
544 the LGM, and the green curve for the higher  $z_0$  (majority of grass, with some shrubs and bare  
545 soil) is more appropriate for a MIS 3 situation. For each of the LGM and MIS 3 simulations  
546 separately, the blue curve can be seen as representing the parts of the domain with scarce  
547 vegetation (mainly the coversands) and the green one, the more vegetated ones – mainly the  
548 loess areas, where part of the dust was trapped.

549

550 As a general evolution, the snow-free fraction of the surface and the depth of dry topsoil are  
551 low in the cold season and high in the warm one (Fig. 17E, F), the important question being to  
552 determine the interval when both variables are high enough to allow significant dust  
553 emissions.

554

555 In both simulations, most of the Landes surface is snow-free all year long. From October to  
556 February the depth of dry topsoil averaged over the domain is too small to allow a significant  
557 dust activity (a 5 mm threshold value was used in Sima et al. 2009). The dusty season could  
558 thus start in the beginning of March. At least for the LGM this is questionable, due to a warm  
559 winter bias causing an underestimation of both snow cover and soil moisture. Indeed, as  
560 mentioned in Banks et al. (2009), the simulated LGM climate over Western Europe is in  
561 agreement with pollen-based reconstructions (Wu et al., 2007) for summer and annual mean  
562 temperatures, and for mean annual precipitation, but winter cooling is underestimated by a  
563 few degrees. Thus, a comparison with the reconstructed directions for dust-efficient winds is  
564 needed to better constrain the beginning of the dusty season. Dust activity is strong until May  
565 or June, decreases to a minimum in July-August (it can even stop in more vegetated parts of  
566 the domain), and may briefly intensify again in September-October before ceasing from  
567 November to February due to unfavourable surface conditions (here soil moisture, in reality  
568 probably also snow).

569

570 In the MIS 3 simulation, the average dry soil depth becomes high enough to allow significant  
571 dust emissions in the beginning of March. Dust activity stops in May due to wind weakening,  
572 which actually may be accentuated by the seasonal development of vegetation, not captured in  
573 the simulation. According to the model, areas with scarce vegetation might continue to emit

574 dust in the beginning of the summer. The simulated winds start to intensify again in autumn,  
575 but the increasing soil moisture plays against a restart of the emissions.

576

## 577 **6. Discussion**

578

### 579 *6.1. Dunes*

580

#### 581 Low amplitude ridges

582

583 The ridges observed in the Gironde district, regardless of their morphology (transverse,  
584 barchanoid), are interpreted as zibars based on their low amplitude and the lack of slipface  
585 (Holm, 1960; Warren, 1972; Tsoar, 1978; Kocurek and Nielson, 1986; Nielson and Kocurek,  
586 1986; Mountney and Russell, 2004). Zibars are often composed of coarse sand and the grain  
587 size is thought to be the main factor involved in preventing the development of a slipface  
588 (Bagnold, 1941; Cooke and Warren, 1973; Nielson and Kocurek, 1986).

589

590 The interpretation of the transverse and barchanoid ridges in the study area as zibars seems to  
591 be the most likely, even if they do not meet all the criteria mentioned above. Indeed, the  
592 zibars of the study area do not show a mode in coarse sands but in medium sands, similar to  
593 that found in parabolic dunes. With regards to dune morphology, we did not find in the  
594 literature zibar examples with a similar range of pattern (transverse, barchanoid, isolated  
595 ridges). Transverse and barchanoid ridges reflect unidirectional winds and point to sand  
596 transport perpendicular to the wind (Pye and Tsoar, 2009), in an environment almost devoid  
597 of vegetation.

598

599 The interpretation of the variations in dune pattern across the coversands is not  
600 straightforward, since the chronological data indicate that the ridge fields developed at  
601 different times: the barchanoid and transverse ridges in the Barp-Cestas area formed during  
602 MIS 4-3, whereas further north the barchanoid ridges date back to the Middle Pleistocene  
603 (Sitzia et al., 2015). Therefore, it remains unclear whether the morphological differences  
604 reflect changes in aeolian dynamics (especially in the availability of sand) during the same  
605 depositional phase or whether they testify to different periods of aeolian deposition.  
606 Nonetheless, it appears that topography, and particularly the slope gradient of the surface on  
607 which the ridges progressed, largely controlled their morphology.

608

609 Parabolic dunes

610

611 Parabolic dunes form in partially vegetated landscapes mainly under unidirectional winds, and  
612 are observed in all latitudes (Lancaster, 1995; Pye and Tsoar, 2009), along sandy coasts (Pye,  
613 1982), but also inland (Sun and Muhs, 2007). They develop mainly from blowouts (Pye and  
614 Tsoar, 2009; Hesp, 2002; Barchyn and Hugenholtz, 2013). The morphology of parabolic  
615 dunes is controlled by the wind strength and direction, the sand supply and the nature of  
616 vegetated ground (Pye, 1982; Pye and Tsoar, 2009; Wolfe et al., 2008). The parabolic dunes  
617 gradually evolve into elongated forms. In some cases, the arms give rise to linear dunes when  
618 the sand supply is low.

619

620 According to available OSL and  $^{14}\text{C}$  ages (Sitzia et al., 2015), the formation of the parabolic  
621 dunes in the Landes area took place mainly during the YD. The clusters of dunes along the  
622 valleys may suggest that the sand was partly supplied by the alluvium. However, the presence  
623 of dune corridors expanding over the plateau and of dunes located on the windward side of  
624 the valleys oriented N-S (e.g. Leyre, Ciron and Avance), testifies unambiguously that the  
625 local fluvial deposits were not the main sand sources. A coastal origin for the sand transported  
626 along the corridors parallel to the wind direction appears to be the most likely.

627

628 The development of dunes along the rivers resulted from the deceleration of the winds  
629 crossing the valleys. Wiggs et al. (2002) proposed the following conceptual model: (1) on the  
630 plateau area above the valley, erosion prevails and sediment accumulation is patchy; (2) on  
631 the windward side of the valley, the wind loses its carrying capacity and sediment tends to  
632 accumulate; (3) on the opposite side of the valley, the wind accelerates and the erosive  
633 potential increases; (4) on the plateau, the wind decelerates again over a short distance  
634 promoting sand deposition. This model correctly explains the dune distribution in the study  
635 area.

636

637 *6.2. Loess sources and transport dynamics*

638

639 The interpolated maps of sand and silt contents suggest a genetic relationship between the  
640 aeolian facies, as previously proposed by Bertran *et al.* (2011, 2016). The distribution of the  
641 contour lines shows a mean NW-SE gradient at the basin scale.

642

643 In the Landes and the Blayais areas, a gradual transition between coarse and fine sand  
644 deposits can be observed, which is not controlled by the nature of the substrate but reflects  
645 wind sorting and/or decreasing carrying capacity as suggested by the distribution of current  
646 mean wind speeds (Fig. 2). The sand-silt transition is mainly controlled by the topographic  
647 change that occurs between the plateau areas (Plateau Girondin, Plateau Landais, Blayais) and  
648 the main valleys (Garonne, Adour and Dordogne). Several authors have already outlined the  
649 role played by topography in the coversand-loess transition, among others Kasse (1997),  
650 Appelman (1956) and Mason et al. (1999). In the southern part of the basin, the transitional  
651 facies (silty sands and sandy silts) form a strip on the right bank of the Adour river, showing  
652 that deposition of the suspended particles was primarily triggered by the expansion of airflows  
653 above the valley. In the northern part of the basin, the transitional facies form a narrower belt  
654 on the left (windward) side of the Garonne valley (Fig. 8), in a context broadly comparable to  
655 the Adour area. In the estuary area to the north, the maps show an almost lack of fine-grained  
656 accumulation on both sides of the valley. The sand-loess transition shifts by approximately 40  
657 km to the east. The abundant ventifacts found on the alluvial terraces point to a deflation-  
658 dominated area.

659

660 The geochemical analysis also strongly suggests a genetic relationship between coversand and  
661 loess. The sand fraction of the southern loess is depleted in K-silicates in comparison with the  
662 coversands and correlatively enriched in quartz and resistant minerals. The enrichment is  
663 especially obvious for Zr and Ti, which concentrate mainly in the fine fraction and tend  
664 broadly to increase as a function of the distance to the coversands. Such a preferential  
665 accumulation of Zr and Ti in loess deposits has been observed worldwide (Gallet et al., 1998;  
666 Scheib et al., 2014) and is interpreted as resulting mainly from grain-size sorting. The recent  
667 alluvial deposits of the Adour river, which are rich in Ca-minerals, did not contribute  
668 significantly to dust production, which derive mainly from the coversands. In the Entre-Deux-  
669 Mers area, the alluvium of the Garonne river provided higher amounts of dust, as suggested  
670 by the larger content of easily alterable minerals in the sand fraction of the loess and, to a  
671 lesser extent, in the fine fraction. Overall, loess appears to be much more homogeneous than  
672 coversand, whose composition is closer to the alluvial sources. We assume that this  
673 homogeneity results from the mixing in the atmosphere of the different dust sources (Gallet et  
674 al., 1998).

675

676 The maps of the thickness of aeolian deposits, which cumulate several sedimentary phases,  
677 provide complementary information. In the northern part of the basin, the thickest loess  
678 deposits are located close to the Garonne valley in the Entre-Deux-Mers area and show rapid  
679 thinning toward the east (Fig. 12A). In the southern area (Fig. 12B), the loess deposits are  
680 mainly located on the left bank of the Adour river and decrease in thickness more gradually  
681 toward both the south and the east. Distinct areas of thick loess accumulation are visible on  
682 the maps but can be, at least in part, an artefact due to kriging using a limited number of data.  
683 The observed pattern of loess thickness can be explained by the following factors:

684

685 (1) The distance to the dust sources. Close to the sources, the decrease in thickness of the  
686 deposits is initially very rapid because the coarser particles, which occupy a large volume,  
687 accumulate at short distances. Farther, the decrease is more gradual and due to lower  
688 concentration of suspended particles in the dust clouds (Simonson and Hutton, 1954;  
689 Waggoner and Bingham, 1961; Frazee et al., 1970). The observed pattern points clearly to the  
690 Sable des Landes Formation and the Blayais sands as the main sources of dust. The rivers  
691 (Dordogne, Lot) flowing from the Massif Central mountains did not provide significant  
692 amounts of dust, as suggested by the lack of variation in loess thickness around the valleys. A  
693 plausible explanation is that armouring developed quickly in the dominantly coarse-grained  
694 alluvial deposits during the Glacial, preventing significant dust entrainment by deflation.

695

696 (2) A change of surface roughness related to the vegetation cover (Tsoar and Pye, 1987). It is  
697 likely that the transition between coversand and loess was associated with a change in plant  
698 cover, which favourable for trapping the particles.

699

### 700 *6.3. Pattern of dust production and accumulation*

701

702 The geochemical analysis shows that northern and southern loess differ substantially in origin.  
703 For the latter, dust derived mainly from aeolian abrasion of the coversands (cf. Wright et al.,  
704 1998; Crouvi et al., 2010). Disconnection of the Landes plateau from the main drainage axes  
705 since at least the early Middle Pleistocene (Sitzia et al. 2015) due to tectonics resulted in  
706 intense redistribution of older alluvial sands by deflation and in the development of  
707 widespread coversands during the successive glacial periods. Repeated remobilization of the  
708 same aeolian sand stock together with fresh inputs from the continental shelf led to  
709 progressive enrichment of the sand material in minerals resistant to alteration (Legigan,

710 1979). The particle transport was predominantly NW-SE and the contribution of the alluvial  
711 plains, mainly oriented perpendicular to the wind, was low. The sand-loess transition is  
712 controlled by topography and coincides with the Adour valley (or the valleys of the  
713 tributaries).

714

715 In the northern part of the basin, dust came from aeolian abrasion of the coversands in the  
716 Blayais and the Plateau Girondin areas, and by deflation of alluvial material from the Garonne  
717 river. Channelling of the winds by the wide Garonne corridor and higher wind speeds  
718 favoured large dust production from the plain. Dust accumulated in the Entre-Deux-Mers area  
719 to form thick deposits mostly restricted to a narrow band on the valley side.

720

721 The loess thickness, which reaches at best 3.5 m in the south and 5 m in the Entre-Deux-Mers  
722 area, is low in comparison with values observed in other European regions (Lautridou, 1985;  
723 Haase et al., 2007). Several factors have been proposed to explain the low rate of  
724 accumulation (Bertran *et al.*, 2011): (1) a limited production of dust by aeolian abrasion of the  
725 coversands; (2) a narrow and steep continental shelf that does not allow storage of large  
726 amounts of fine alluvial sediment in the Garonne valley during sea lowstands; (3) a high soil  
727 moisture and, therefore, a low ground susceptibility to wind erosion due to an oceanic climate.  
728 The palaeoclimatic simulations both for LGM and MIS 3 agree to show that the average  
729 rainfall was significantly higher near the Atlantic coast than in Eastern Europe (Laîné et al.,  
730 2009; Kjellstrom et al., 2010; Strandberg *et al.*, 2011; Sima et al., 2013) where much thicker  
731 loess deposits accumulated. However, this role remains questionable insofar as the  
732 reconstructed maximum in rainfall occurred in the winter season, which did not necessarily  
733 correspond to the most favourable period of aeolian transport.

734

#### 735 *6.4. Last-glacial wind regime from data and model constraints*

736

737 The grain-size gradient together with the orientation of low-amplitude ridges and parabolic  
738 dunes allow reconstructing the prevailing wind directions of aeolian transport during the Last  
739 Glacial and the Lateglacial (Fig. 17A). The transverse ridges of the Plateau Girondin area  
740 dated to MIS 4-3 indicate efficient winds from the W. Some variability exists but appears to  
741 result from local topographical factors and from channelling of the air masses along the  
742 Garonne corridor. Unfortunately, the almost lack of MIS 2 ridge fields visible in aerial  
743 photographs does not allow getting data for this period. The crests of the MIS 2 ridges

744 illustrated in Figure 4 are oriented W-E, and indicate local efficient winds blowing from the  
745 north. At the basin scale the contour lines of the grain size point to winds originating from the  
746 W or the NW, and are assumed to reflect the mean direction of efficient winds during the  
747 glacial. Finally, the parabolic dunes attest for winds coming from the W-SW during the YD.  
748 The following considerations must be taken into account with regard to the reconstruction of  
749 wind directions:

750

751 (1) The accuracy of the geological proxies used may vary. The dunes are considered as the  
752 best marker for the reconstruction of past wind circulation patterns (Lancaster, 1990),  
753 especially when dunes formed under unidirectional winds (Marrs and Kolm, 1982). With  
754 regard to grain-size gradients, Renssen et al. (2007) suggested that a significant uncertainty is  
755 associated with this type of feature. The analysis made here across the Aquitaine basin,  
756 however, shows a good consistency in the regional distribution of the contour lines.

757

758 (2) The reconstructed directions of aeolian transport are indicative of the wind regimes at the  
759 regional scale during the periods of accumulation. In most of the modern sand seas, the axis  
760 of unidirectional dunes is oriented perpendicular (e.g. barchan, transverse ridges, parabolic  
761 dunes) to the dominant wind direction, i.e. the direction with the highest transport rate of sand  
762 (Fryberger and Dean, 1979). Seasonal fluctuations in wind strength are assumed to be the  
763 main factor involved in modulating the intensity of deflation. In periglacial environments,  
764 however, wind intensity is not the only factor that controls the season of aeolian transport.  
765 Other factors, particularly the snow cover and soil moisture, play a significant role on the  
766 susceptibility of the ground to deflation (Koster, 1988; Seppälä, 2004). Depending on the  
767 temperature and precipitation regimes (also determining the vegetation), different situations  
768 exist. In cold and arid environments, based on observations in the Søndre Strømfjord region  
769 (West Greenland), Dijkmans and Törnqvist (1991) have shown that aeolian transport occurred  
770 mainly during part of the winter season, whereas summer was less favourable to deflation  
771 because of vegetation growth and ground-ice melting. Based on laboratory experiments,  
772 McKenna-Neuman (1989) also showed that the release of sand material susceptible to be  
773 transported by the wind can very active when the temperature drops below  $-20^{\circ}\text{C}$  because of  
774 ice sublimation. On the contrary, between  $-5$  and  $-15^{\circ}\text{C}$ , the erosion threshold increases  
775 considerably due to the presence of a significant amount of liquid water in the ground.  
776 Dijkmans and Koster (1990), for Alaska, underline that when the snow cover is thick, the  
777 season of aeolian transport shifts towards the end of winter. According to Seppälä (2004), in



778 arctic and subarctic regions where snow is abundant, deflation is effective only during  
779 summer, i.e. after snowmelt.

780

781 In the following, we compare our proxy data and palaeoclimatic simulations in an attempt to  
782 specify the periods of the year when dust activity occurred during the investigated climate  
783 intervals. The result depends on how reliable the simulated variables, especially the wind  
784 directions, are. In the region studied here, the atmospheric circulation is largely determined by  
785 the surface conditions (temperatures, sea-ice extent) in the North Atlantic; in glacial times,  
786 another key factor was the size of the Laurentide ice sheet (e.g., Löffverström et al., 2014,  
787 Beghin et al., 2015). In our simulation for 21 ka, these elements are imposed from  
788 reconstructions for the LGM (GLAMAP, ICE-5G). Even though these reconstructions have  
789 their uncertainties, we tend to be confident in the general aspect of the modelled annual cycle  
790 of wind directions. For the 39 ka simulation, the sea-level drop is realistic and the ice-sheet  
791 configuration is adapted to this sea-level drop, the main uncertainty being related to the  
792 North-Atlantic surface conditions. Results of numerical experiments with the LOVECLIM  
793 earth system model of intermediate complexity (Van Meerbeek et al., 2009) show a  
794 difference of air temperature of 3°C on average over the North Atlantic between an average  
795 MIS 3 stadial state and the LGM. For the MIS 3 run examined here, the difference is 2.5°C,  
796 close enough to the Van Meerbeek et al. value, knowing that there was no unique (or  
797 average) MIS 3 stadial climate, but many stadial episodes differing in ice-sheet size and  
798 orbital parameters.

799

800 Since we are reasonably confident in the simulated wind directions, constraints on the dusty  
801 season can be derived using the comparison between the modelled wind directions and those  
802 reconstructed from field proxies, together with the results of sensitivity experiments with  
803 lower roughness length more typical of glacial vegetation. The only other constraining  
804 element that we can use is the simulated soil moisture, keeping in mind that it is  
805 underestimated in the cold part of the year.

806

807 In the LGM simulation, soil moisture conditions allow dust activity to start in the beginning  
808 of March, while reconstructed W-NW wind directions suggest that the dusty season should  
809 not begin before mid-March, when simulated winds change from W-SW to W (Fig. 17A).  
810 Sand transport took place during the spring/summer times because of scarce vegetation,  
811 adequate wind speeds and well-drained sandy soils. According to recent investigations

812 (Andrieux et al., 2016), permafrost, which might have impeded drainage (Kasse, 1997), was  
813 lacking during most of the period of sand accumulation. Deflation may have been more  
814 restricted in summer in the loess area because of the denser vegetation cover. This scenario  
815 contrasts with that proposed by Renssen et al. (2007) for more northern latitudes, which  
816 suggested winter to be the most suitable period for deflation during MIS 2. In such a  
817 permafrost context and by comparison with the modern periglacial environments investigated  
818 by Dijkmans (1990) and Dijkmans and Törnqvist (1991), deflation was thought to have been  
819 impeded during the summer because the ground was mostly wet (thaw of the active layer),  
820 vegetation was growing, and the wind speeds were lower than in the winter season. It is worth  
821 noting that the observations in modern milieus were made on aeolian systems supplied by  
822 proglacial rivers. These rivers fed by glaciers are mostly active after the spring melt. In  
823 summer, the water table rises and, as a consequence, the sediment availability to deflation is  
824 low (Mountney and Russell, 2009). Such an aeolian system was probably characteristic of the  
825 margins of the Scandinavian ice sheet (Koster, 1988), but cannot be transposed to regions far  
826 from an ice sheet such as the Aquitaine basin. In this oceanic region, the ground was wet and  
827 largely protected by a snow cover (largely underestimated in our simulation) during the  
828 passage of winter storms, but dried in summer, thus becoming more susceptible for deflation.

829

830 In the MIS 3 simulation, the soil becomes dry enough in the beginning of March, while the  
831 reconstructed westerly winds suggest that the dusty season should not begin before the end of  
832 March. Both data and model agree that the dust activity should cease in the end of May, when  
833 the simulated winds turn from W (which is the reconstructed direction) to WNW, and the  
834 maximum wind speeds, recalculated with a roughness length value more typical of steppe  
835 vegetation (green curve in Fig. 17D), become too weak. The modelled wind directions  
836 coincide again with the reconstructed (westerly) ones in autumn, but the simulated increase in  
837 soil moisture suggests that little, if any, dust activity should occur.

838

839 Wind strength, soil moisture and snow cover determine the dusty season(s) in scarcely  
840 vegetated environments, Where vegetation has strong seasonal variations, its impact is also  
841 important. The developing vegetation contributes to wind weakening through increasing  
842 roughness length, and protects the surface against erosion, The later effect cannot be  
843 estimated here due to the unrealistically high vegetation cover in the study region, but Sima et  
844 al. (2009) have found that it stopped dust activity in the warm season under MIS 3 conditions  
845 in Europe at latitudes around 50°N.

846

847 We do not have a simulation for the YD, but we note that the annual cycle of wind direction  
848 does not considerably change between present day, LGM and MIS 3 (in our simulations, also  
849 in those by van Huissteden and Pollard 2003), and even from the present day. Therefore, we  
850 may speculate that winter, typified by dominantly W-SW wind directions, was the main  
851 period of sand transport during the YD. In Western Europe, winter is the season that  
852 corresponds to the passage of the main perturbations and associated storms, and that records  
853 the highest wind speeds (Fig. 17C, D). These wind directions are in agreement with those  
854 reconstructed for the YD by Isarin et al. (1997). The YD orientation of parabolic dunes in  
855 Aquitaine is identical to that observed in the Netherlands (Isarin et al., 1997) and should be  
856 associated with increased speed of SW winds throughout Northwestern and Western Europe  
857 (Isarin et al., 1997). Differences should have been important in the surface conditions, which  
858 for the YD allowed dust activity in winter: scarce vegetation, reduced snow cover compared  
859 to LGM and MIS 3, and reduced soil moisture favoured by improved ground drainage due to  
860 the lack of permafrost and to the weaker influence of meltwater from the ice sheets (for  
861 Northern Europe).

862

863

## 864 **7. Conclusions**

865

866 The multi-approach study of the aeolian deposits of southwest France allows better  
867 understanding of sediment sources and depositional dynamics. The maps of interpolated grain  
868 size and the geochemical composition converge to show a genetic relationship between  
869 coversands and finer-grained deposits. In the southern part of the basin, dust derived mainly  
870 from aeolian abrasion of the coversands and is dominantly composed of minerals resistant to  
871 alteration. In contrast, both the coversands and the floodplain of the Garonne river, richer in  
872 Ca-bearing minerals, contributed to loess in the northern part of the basin.

873

874 The low-amplitude dunes lacking slipfaces, dated to MIS 4-3, are interpreted as zibars and  
875 show variable morphologies (transverse, barchanoid, isolated barchanoid) occurring as strips  
876 subparallel to the coastline. This pattern seems to be mainly controlled by the slope gradient.  
877 The parabolic dunes dated to the YD are simple, complex or compound. These are clustered  
878 along the rivers but are rare on the plateaus, which correspond to deflation areas. In the  
879 valleys oriented W-E, i.e. parallel to the prevailing winds, corridors of elongated parabolic

880 dunes developed, whereas more simple shapes occur on both sides of the valleys  
881 perpendicular to the winds. These formed as a consequence of relief-induced deceleration of  
882 the airflows. Overall, the dune distribution indicates that the sand supply came mainly from  
883 the coast.

884

885 The spatial analysis of dune shapes and grain-size gradients, as well as the study of dust  
886 sources, made it possible reconstructing the Last Glacial wind regimes in the study region.  
887 The efficient winds changed significantly through time. They came from the W to the NW  
888 during the glacial, and the W-SW during the YD. The comparison between proxy data and  
889 both the current and simulated Last Glacial wind regimes strongly suggests that aeolian  
890 transport of sand and dust occurred mostly during the spring/summer season for the glacial,  
891 and the winter for the YD. We assume that these variations were not related to changes in the  
892 pattern of atmospheric circulation, but rather to changes in the deflation season. This was  
893 mainly controlled by the length of the season with a snow cover and frozen or moist ground,  
894 and by the seasonal evolution of the wind speeds able to cause deflation. Vegetation could  
895 impose additional constraints in areas or periods when its seasonal variations were significant.

896

## 897 **Acknowledgments**

898

899 We acknowledge Christophe Tuffery (Inrap) for his help in the GIS. This work was funded by  
900 Inrap, the University of Bordeaux and Lascarb (Universités de Bordeaux, program of the  
901 Agence Nationale de la Recherche ANR-10-LABX-52). The Labex L-IPSL, which is funded  
902 by the ANR (grant #ANR-10-LABX-0018), is also acknowledged. The two anonymous  
903 reviewers are also thanked for their remarks, which contributed to greatly improve the  
904 manuscript. The simulations used here have been run on the HPC facilities of the  
905 Commissariat à l'Energie Atomique.

906

## 907 **References**

908

909 Aitchison, J., 1982. The Statistical Analysis of Compositional Data. *Journal of the Royal*  
910 *Statistical Society, series B (Methodological)* 44, 139–177.

911

912 Aitchison, J., 1986. *The Statistical Analysis of Compositional Data*. Chapman & Hall,  
913 London, UK, 416 pp.

914

915 Aitchison, J., Greenacre, M., 2002. Biplots of compositional data. *Journal of the Royal*  
916 *Statistical Society, series C (Applied Statistics)* 51, 375–392.

917

918 Andrieux, E., Bertran, P., and Saito, K., 2016. Spatial analysis of the French Pleistocene  
919 permafrost by a GIS database. *Permafrost and Periglacial Processes* 27, 17–30.

920

921 Antoine, P., Rousseau, D.-D., Zöller, L., Lang, A., Munaut, A.-V., Hatté, C., Fontugne, M.,  
922 2001. High-resolution record of the last Interglacial-glacial cycle in the Nussloch loess-  
923 palaeosol sequences, Upper Rhine Area, Germany. *Quaternary International* 76-77, 211–229.

924

925 Appelman F., 1956. Variation de la composition granulométrique des sédiments éoliens en  
926 rapport avec leur latitude et leur altitude. *Pédologie* VI, 26–37.

927

928 Ballabio, C., Panagos, P., Monatanarella, L., 2016. Mapping topsoil physical properties at  
929 European scale using the LUCAS database. *Geoderma* 261, 110-123.

930

931 Bagnold, R.A., 1941. *The physics of wind blown sand and desert dunes*. Methuen, London,  
932 265 pp.

933

934 Banks, W. E., Zilhão, J., d'Errico, F., Kageyama, M., Sima, A., & Ronchitelli, A. (2009).  
935 Investigating links between ecology and bifacial tool types in Western Europe during the Last  
936 Glacial Maximum. *Journal of Archaeological Science*, 36, 2853-2867.

937

938 Barchyn, T.E., Hugenholtz, C.H., 2013. Reactivation of supply-limited dune fields from  
939 blowouts: A conceptual framework for state characterization. *Geomorphology* 201, 172–182.

940

941 Berger, A., 1978. Long-term variations of caloric solar radiation resulting from the earth's  
942 orbital elements. *Quaternary Research* 9, 139–167.

943

944 Bertran, P., Allenet, G., Gé, T., Naughton, F., Poirier, P., Goñi, M.F.S., 2009. Coversand and  
945 Pleistocene palaeosols in the Landes region, southwestern France. *Journal of Quaternary*  
946 *Science* 24, 259–269.

947

948 Bertran, P., Bateman, M.D., Hernandez, M., Mercier, N., Millet, D., Sitzia, L., Tastet, J.-P.,  
949 2011. Inland aeolian deposits of south-west France: facies, stratigraphy and chronology.  
950 *Journal of Quaternary Science* 26, 374–388.  
951

952 Bertran, P., Andrieux, E., Antoine, P., Coutard, S., Deschodt, L., Gardère, P., Hernandez, M.,  
953 Legentil, C., Lenoble, A., Liard, M., Mercier, N., Moine, O., Sitzia, L., Van Vliet-Lanoë, B.,  
954 2013. Distribution and chronology of Pleistocene permafrost features in France: database and  
955 first results. *Boreas* 43. 699-711.  
956

957 Bertran, P., Liard, M., Sitzia, L., Tissoux, H., 2016. A map of Pleistocene aeolian deposits in  
958 Western Europe, with special emphasis on France. *Journal of Quaternary Science* 31 (8), 844-  
959 856.  
960

961 Braconnot, P., 2004. Modeling the last glacial maximum and mid-holocene. *Comptes Rendus*  
962 *Geoscience* 336, 711–719.  
963

964 Buurman, P., Pape, T., Reijneveld, J.A., de Jong, F., van Gelder, E., 2001. Laser-diffraction  
965 and pipette-method grain sizing of Dutch sediments: correlations for fine fractions of marine,  
966 fluvial, and loess samples. *Netherlands Journal of Geosciences* 80, 49-57.  
967

968 Capdeville J.-P., Dubreuilh J., 1994. Les formations superficielles du Bassin d'Aquitaine:  
969 identification, potentialités, contraintes. BRGM report R-38 271, Orléans, 52 pp.  
970

971 Comas-Cufí, M., Thió-Henestrosa, S., 2011. CoDaPack 2.0: A stand-alone, multi-platform  
972 compositional software. <http://ima.udg.edu/codapack/> (accessed 06/07/2016).  
973

974 Conseil régional Aquitaine et ADEME Aquitaine, 2008. Cartographie du gisement éolien, des  
975 contraintes et servitudes en Aquitaine, Unpublished Report, 27 pp.  
976

977 Cooke, R.U., Warren, A., 1973. *Geomorphology in Deserts*. University of California Press,  
978 448 pp.  
979

980 Crouvi, O., Amit, R., Enzel, Y., Gillespie, A.R., 2010. Active sand seas and the formation of  
981 desert loess. *Quaternary Science Reviews* 29, 2087–2098.

982

983 De Vos, W., Tarvainen, T., Salminen, R., Reeder, S., De Vivo, B., Demetriades, A., Pirc, S.,  
984 Batista, M.J., Marsina, K., Ottesen, R.T., O'Connor, P.J., Bidovec, M., Lima, A., Siewers, U.,  
985 Smith, B., Taylor, H., Shaw, R., Salpeteur, I., Gregorauskiene, V., Halamic, J., Slaninka, I.,  
986 Lax, K., Gravesen, P., Birke, M., Breward, N., Ander, E.L., Jordan, G., Duris, M., Klein, P.,  
987 Locutura, J., Bel-lan, A., Pasieczna, A., Lis, J., Mazreku, A., Gilucis, A., Heitzmann, P.,  
988 Klaver, G., Petersell, V., 2006. Geochemical Atlas of Europe. Part 2 - Interpretation of  
989 Geochemical Maps, Additional Tables, Figures, Maps, and Related Publications, Geological  
990 Survey of Finland, Espoo.

991

992 Dijkmans, J.W.A., Koster, E.A., 1990. Morphological Development of Dunes in a Subarctic  
993 Environment, Central Kobuk Valley, Northwestern Alaska. *Geografiska Annaler. Series A,*  
994 *Physical Geography* 72, 93–109.

995

996 Dijkmans, J.W.A., Törnqvist, T.E., 1991. Modern periglacial eolian deposits and landforms in  
997 the Søndre Strømfjord area, West Greenland and their palaeoenvironmental implications.  
998 *Meddelelser om Grønland. Geoscience* 25, 3–39.

999

1000 Dubreuilh, J., 1976. Contribution à l'étude sédimentologique du système fluvial Dordogne-  
1001 Garonne dans la région bordelaise. Thèse d'état, Université de Bordeaux, Bordeaux, 273 pp.

1002

1003 Dubreuilh, J., Capdeville, J.P., Farjanel, G., Karnay, G., Platel, J.P., Simon-Coinçon, R.,  
1004 1995. Dynamique d'un comblement continental néogène et quaternaire: l'exemple du bassin  
1005 d'Aquitaine. *Géologie de la France* 4, 3–26.

1006

1007 Duchaufour, P., 1997. *Abrégé de pédologie : sol, végétation, environnement.* Masson, Paris,  
1008 285 pp.

1009

1010 Enjalbert, H., 1960. *Les Pays Aquitains : Le modelé et les sols.* Imprimerie Bière, Bordeaux.

1011

1012 Egozcue J., Pawlowsky-Glahn, V., Mateu-Figueras, G., Barcelo'- Vidal, C., 2003. Isometric  
1013 logratio transformations for compositional data analysis. *Mathematical Geology* 35, 3, 279–  
1014 300.

1015

1016 Ewing, R.C., Kocurek, G., Lake, L.W., 2006. Pattern analysis of dune - field parameters.  
1017 Earth Surface Processes and Landforms 31, 1176–1191.  
1018

1019 Fralick B.W., Kronberg B.I., 1997. Geochemical discrimination of clastic sedimentary rock  
1020 sources. Sedimentary Geology 113, 111-124.  
1021

1022 Frazee, C.J., Fehrenbacher, J.B., Krumbein, W.C., 1970. Loess Distribution from a Source.  
1023 Soil Science Society of America Journal 34, 296–301.  
1024

1025 Fryberger, S.G., Dean, G., 1979. Dune forms and wind regime, in: McKee, E.D. (Ed.), A  
1026 Study of Global Sand Seas, Geological Survey Professional Paper 1052, United States  
1027 Government Printing Office Washington DC, p. 137–171.  
1028

1029 Gallet, S., Jahn, B., Van Vliet Lanoë, B., Dia, A., Rossello, E., 1998. Loess geochemistry and  
1030 its implications for particle origin and composition of the upper continental crust. Earth and  
1031 Planetary Science Letters 156, 157–172.  
1032

1033 Haase, D., Fink, J., Haase, G., Ruske, R., Pécsi, M., Richter, H., Altermann, M., Jäger, K.-D.,  
1034 2007. Loess in Europe--its spatial distribution based on a European Loess Map, scale  
1035 1:2.500.000. Quaternary Science Reviews 26, 1301–1312.  
1036

1037 Hernandez, M., Mercier, N., Bertran, P., Colonge, D., Lelouvier, L.A., 2012. Premiers  
1038 éléments de datation des industries du Pléistocène moyen (Acheuléen - Paléolithique moyen  
1039 ancien) de la région pyrénéo-garonnaise : une approche géochronologique pluri-méthodes  
1040 (TL, OSL et TT-OSL) des sites de Duclos et Romentères. Paléo 23, 155–170.  
1041

1042 Hesp, P., 2002. Foredunes and blowouts: initiation, geomorphology and dynamics.  
1043 Geomorphology 48, 245–268.  
1044

1045 Holm, D.A., 1960. Desert Geomorphology in the Arabian Peninsula. Science 132, 1369–  
1046 1379.  
1047

1048 INRA, 2011. Donesol version 2.0.5. [http://acklins.orleans.inra.fr/outil/donesol/dictionnaire\\_](http://acklins.orleans.inra.fr/outil/donesol/dictionnaire_)  
1049 [donesol\\_igcs\\_2011-02-25.pdf](http://acklins.orleans.inra.fr/outil/donesol/dictionnaire_donesol_igcs_2011-02-25.pdf) (accessed 05.07.2016).



1050

1051 Isarin, R.F.B., Renssen, H., Koster, E.A., 1997. Surface wind climate during the Younger  
1052 Dryas in Europe as inferred from aeolian records and model simulations. *Palaeogeography,*  
1053 *Palaeoclimatology, Palaeoecology* 134, 127-148.

1054

1055 Karnay, G., Corbier, P., Bourguine, B., Saltel M., 2010. Gestion des eaux souterraines en  
1056 région Aquitaine. Reconnaissance des potentialités aquifères du Mio-Plio-Quaternaire des  
1057 Landes de Gascogne et du Médoc en relation avec les SAGE. BRGM report RP 57813,  
1058 Orléans, 73 pp.

1059

1060 Kasse, C., 1997. Cold-Climate Aeolian Sand-Sheet Formation in North-Western Europe (c.  
1061 14–12.4 ka); a Response to Permafrost Degradation and Increased Aridity. *Permafrost and*  
1062 *Periglacial Processes* 8, 295–311.

1063

1064 Kjellström, E., Brandefelt, J., Näslund, J.-O., Smith, B., Strandberg, G., Voelker, A. H. L.,  
1065 Wohlfarth, B., 2010. Simulated climate conditions in Europe during the Marine Isotope Stage  
1066 3 stadial. *Boreas* 39: 436–456.

1067

1068 Klingebiel, A., 1966. Observations sur les sables de recouvrement superficiel dans le  
1069 bordelais. *Bulletin de la carte géologique de la France*, t. LXI, 278, 185–188.

1070

1071 Kocurek, G., Nielson, J., 1986. Conditions favourable for the formation of warm-climate  
1072 aeolian sand sheets. *Sedimentology* 33, 795–816.

1073

1074 Konert, M., Vandenberghe, J., 1997. Comparison of laser grain size analysis with pipette and  
1075 sieve analysis: a solution for the underestimation of the clay fraction. *Sedimentology* 44, 523–  
1076 535.

1077

1078 Koster, E.A., 1988. Ancient and modern cold-climate aeolian sand deposition: A review.  
1079 *Journal of Quaternary Science* 3, 69–83.

1080

1081 Krinner, G., Viovy, N., de Noblet-Ducoudré, N., Ogée, J., Polcher, J., Friedlingstein, P.,  
1082 Ciais, P., Sitch, S., Prentice, I.C., 2005. A dynamic global vegetation model for studies of the  
1083 coupled atmosphere-biosphere system. *Global Biogeochemical Cycles* 19, GB1015.

1084

1085 Kutzbach, J.E., Wright Jr., H.E., 1985. Simulation of the climate of 18,000 years BP: results  
1086 for the North American/North Atlantic/European sector and comparison with the geologic  
1087 record of North America. *Quaternary Science Reviews* 4, 147–187.

1088

1089 Laine A., Kageyama M., Salas-Mélia D., Valdoire A., Rivière G., Ramstein G., Planton S.,  
1090 Tyteca S., Peterschmidt J.Y., 2009. Northern Hemisphere storm tracks during the last glacial  
1091 maximum in the PMIP2 ocean-atmosphere coupled models: energy study, seasonal cycle,  
1092 precipitation. *Climate Dynamics* 32, 593-614.

1093

1094 Lancaster, N., 2008. Desert dune dynamics and development: insights from luminescence  
1095 dating. *Boreas* 37, 559–573.

1096

1097 Lancaster, N., 1995. *Geomorphology of desert dunes*. Routledge physical environment series,  
1098 K. Richards (ed.), Routledge, London, New York, 290 pp.

1099

1100 Lancaster, N., 1990. Palaeoclimatic evidence from sand seas. *Palaeogeography,*  
1101 *Palaeoclimatology, Palaeoecology* 76, 279–290.

1102

1103 Lancaster, N., Kocurek, G., Singhvi, A., Pandey, V., Deynoux, M., Ghienne, J.-F., Lo, K.,  
1104 2002. Late Pleistocene and Holocene dune activity and wind regimes in the western Sahara  
1105 Desert of Mauritania. *Geology* 30, 991–994.

1106

1107 Lautridou, J.-P., 1985. *Le cycle périglaciaire pleistocène en Europe du nord-ouest et plus*  
1108 *particulièrement en Normandie*. Thèse d'état, Université de Caen, Centre de géomorphologie  
1109 du C.N.R.S, Caen, France, 908 pp.

1110

1111 Léger, M., 1990. Loess landforms. *Quaternary International* 7/8, 53-61.

1112

1113 Legigan, P., 1979. *L'élaboration de la formation du Sable des Landes*, Mémoire de l'Institut  
1114 de Géologie du Bassin d'Aquitaine, Bordeaux, 429 pp.

1115

1116 Liu, T., 1988. *Loess in China*. Springer series in physical environment, Springer, Berlin, 224  
1117 pp.

1118

1119 Löffverström, M., Caballero, R., Nilsson, J., Kleman, J., 2014. Evolution of the large-scale  
1120 atmospheric circulation in response to changing ice sheets over the last glacial cycle, *Climate*  
1121 *of the Past* 10, 1453-1471, doi: 10.5194/cp-10-1453-2014.

1122

1123 Maarleveld, G.C., 1960. Wind directions and cover sands in the Netherlands. *Biuletyn*  
1124 *Peryglacjalny* 8, 49–58.

1125

1126 Marrs, R.W., Kolm, K.E. (Eds.), 1982. Interpretation of windflow characteristics from eolian  
1127 landforms, Special paper 192, Geological society of America, Boulder, USA, 109 pp.

1128

1129 Martín-Fernández, J., Barceló-Vidal, C., Pawlowsky-Glahn, V., 2003. Dealing with Zeros and  
1130 Missing Values in Compositional Data Sets Using Nonparametric Imputation. *Mathematical*  
1131 *Geology* 35, 253–278.

1132

1133 Mason, J.A., 2001. Transport Direction of Peoria Loess in Nebraska and Implications for  
1134 Loess Sources on the Central Great Plains. *Quaternary Research* 56, 79–86.

1135

1136 Mason, J.A., Nater, E.A., Zanner, C.W., Bell, J.C., 1999. A new model of topographic effects  
1137 on the distribution of loess. *Geomorphology* 28, 223–236.

1138

1139 McKee, E.D., 1979. Introduction to a study of global sand seas, in: E.D. McKee (ed.), *A*  
1140 *Study of Global Sand Seas*, Geological Survey Professional Paper 1052, United States  
1141 Government Printing Office Washington DC, pp. 1–19.

1142

1143 McKenna Neuman, C., 1989. Kinetic energy transfer through impact and its role in  
1144 entrainment by wind of particles from frozen surfaces. *Sedimentology* 36, 1007–1015.

1145

1146 Melkerud P.A., Bain D.C., Jongmans A.G., Tarvainen T., 2000. Chemical, mineralogical and  
1147 morphological characterization of three podzols developed on glacial deposits in Northern  
1148 Europe. *Geoderma* 94, 125-148.

1149

1150 Mountney, N.P., Russell, A.J., 2009. Aeolian dune - field development in a water table  
1151 controlled system: Skeiðarársandur, Southern Iceland. *Sedimentology* 56, 2107–2131.

1152

1153 Muhs, D.R., Bettis, E.A., Aleinikoff, J.N., McGeehin, J.P., Beann, J., Skipp, G., Marshall,  
1154 B.D., Roberts, H.M., Johnson, W.C., Benton, R., 2008. Origin and paleoclimatic significance  
1155 of late Quaternary loess in Nebraska: Evidence from stratigraphy, chronology, sedimentology,  
1156 and geochemistry. *Geological Society of America Bulletin* 120, 1378–1407.

1157

1158 Nielson, J., Kocurek, G., 1986. Climbing Zibars of the Algodones. *Sedimentary Geology* 48,  
1159 1–15.

1160

1161 Pannatier, Y., 1996. *Variowin: software for spatial data analysis in 2D*, Statistics and  
1162 computing. Springer, New York, Berlin, London, Paris, 91 pp.

1163

1164 Park, S.-U., In, H.-J., 2003. Parameterization of dust emission for the simulation of the  
1165 Yellow Sand (Asian dust) observed in March 2002 in Korea. *Journal of Geophysical Research*  
1166 108, 4618, doi:10.1029/2003JD003484.

1167

1168 Paul, A., Schäfer-Neth, C., 2003. Modeling the water masses of the Atlantic Ocean at the Last  
1169 Glacial Maximum. *Paleoceanography* 18, 1058.

1170

1171 Pawlowsky-Glahn, V., Buccianti, A., 2011. *Compositional Data Analysis: Theory and*  
1172 *Applications*. John Wiley & Sons, Chichester, 378 pp.

1173

1174 Pawlowsky-Glahn, V., Olea, R.A., 2004. *Geostatistical analysis of compositional data*.  
1175 Oxford University Press, Oxford, 204 pp.

1176

1177 Pawlowsky, V., Burger, H., 1992. Spatial structure analysis of regionalized compositions.  
1178 *Mathematical Geology* 24, 675–691.

1179

1180 Peltier W.R., 2004. Global glacial isostasy and the surface of the ice-age earth: the ICE-5G  
1181 (VM2) Model and GRACE Annual Review of Earth and Planetary Sciences 32, 111-149.

1182

1183 Poser, H., 1950. Zur Rekonstruktion der spätglazialen Luftdruckverhältnisse in Mittelund  
1184 Westeuropa auf Grund der vorzeitlichen binnendünen. *Erdkunde* 4, 81–88.

1185

1186 Pye, K., 1982. Morphological Development of Coastal Dunes in a Humid Tropical  
1187 Environment, Cape Bedford and Cape Flattery, North Queensland. *Geografiska Annaler*.  
1188 Series A, Physical Geography 64, 213–227.  
1189

1190 Pye, K., Tsoar, H., 2009. *Aeolian sand and sand dunes*. Springer, Berlin, Heidelberg, 458 pp.  
1191

1192 Raynaud, D., Jouzel, J., Barnola, J.M., Chapellaz, J., Delmas, R.J., Lorius, C., 1993. The ice  
1193 record of greenhouse gases. *Science* 259, 926–934.  
1194

1195 Reimann C., Demetriades A., Birke M., Filzmoser P., O’Connor P., Halamić J., Ladenberger  
1196 A., The GEMAS Project Team, 2014. Distribution of elements/parameters in agricultural and  
1197 grazing land soil of Europe. In C. Reimann, M. Birke, A. Demestriades, P. Filzmoser & P.  
1198 O’Connor, *Chemistry of Europe’s agricultural soils, Part A: Methodology and interpretation*  
1199 *of the GEMAS Data Set*, *Geologisches Jahrbuch, Reihe B*, 102, 103-523.  
1200

1201 Renssen, H., Kasse, C., Vandenberghe, J., Lorenz, S.J., 2007. Weichselian Late Pleniglacial  
1202 surface winds over northwest and central Europe: a model–data comparison. *Journal of*  
1203 *Quaternary Science* 22, 281–293.  
1204

1205 Righi D., De Coninck F., 1974. Micromorphological aspects of Humods and Haplaquods of  
1206 the Landes du Médoc, France. in: Rutherford, G.K. (Ed.), *Soil Microscopy*. Limestone Press,  
1207 Kingston, Ontario, pp. 567– 588.  
1208

1209 Rousseau D.D., Chauvel C., Sima A., Hatté C., Lagroix F., Antoine P., Balkanski Y., Fuchs  
1210 M., Mellett C., Kageyama M., Ramstein G., Lang A., 2014. European Glacial Dust Deposits:  
1211 Geochemical Constraints on Atmospheric Dust Cycle Modeling. *Geophysical Research*  
1212 *Letters* 41, 7666-7674. doi : 10.1002/2014GL061382  
1213

1214 Ruegg, G.H.J., 1983. Periglacial Eolian Evenly Laminated Sandy Deposits in the Late  
1215 Pleistocene of Nw Europe, A Facies Unrecorded in Modern Sedimentological Handbooks, in:  
1216 *Developments in Sedimentology*. Elsevier, pp. 455–482.  
1217

1218 Sarnthein, M., Gersonde, R., Niebler, S., Pflaumann, U., Spielhagen, R., Thiede, J., Wefer,  
1219 G., Weinelt, M., 2003. Overview of Glacial Atlantic Ocean Mapping (GLAMAP 2000).  
1220 *Paleoceanography* 18, 1030.  
1221

1222 Scheib A.J., Birke M., Dinelli E., GEMAS Project Team, 2014. Geochemical evidence of  
1223 aeolian deposits in European soils. *Boreas* 43, 175-192.  
1224

1225 Schwan, J., 1986. The origin of horizontal alternating bedding in weichselian aeolian sands in  
1226 Northwestern Europe. *Sedimentary Geology* 49, 73–108.  
1227

1228 Seppälä, M., 2004. Wind as a geomorphic agent in cold climates. Cambridge University press,  
1229 Cambridge, 358 pp..  
1230

1231 Sima, A., Rousseau, D.-D., Kageyama, M., Ramstein, G., Schulz, M., Balkanski, Y., Antoine,  
1232 P., Dulac, F., Hatté, C., 2009. Imprint of North-Atlantic abrupt climate changes on western  
1233 European loess deposits as viewed in a dust emission model. *Quaternary Science Reviews* 28,  
1234 2851–2866.  
1235

1236 Sima, A., Kageyama, M., Rousseau, D.-D., Ramstein, G., Balkanski, Y., Antoine, P., and  
1237 Hatté, C., 2013. Modeling dust emission response to North Atlantic millennial-scale climate  
1238 variations from the perspective of East European MIS 3 loess deposits, *Climate of the Past* 9,  
1239 1385-1402.  
1240

1241 Simonson R.W., Hutton C.E., 1954. Distribution curves for loess. *American Journal of*  
1242 *Science* 252, 99–105.  
1243

1244 Sitzia, L., 2014. Chronostratigraphie et distribution spatiale des dépôts éoliens du Bassin  
1245 Aquitain. PhD Thesis, Université de Bordeaux, Bordeaux, 341 pp.  
1246

1247 Sitzia, L., Bertran, P., Bahain, J.-J., Bateman, M.D., Hernandez, M., Garon, H., de Lafontaine,  
1248 G., Mercier, N., Leroyer, C., Queffelec, A., Voinchet, P., 2015. The Quaternary coversands of  
1249 southwest France. *Quaternary Science Reviews* 124, 84–105.  
1250

1251 Stevens, T., Palk, C., Carter, A., Lu, H., Clift, P.D., 2010. Assessing the provenance of loess  
1252 and desert sediments in northern China using U-Pb dating and morphology of detrital zircons.  
1253 Geological Society of America Bulletin 122, 1331–1344.  
1254

1255 Strandberg G., Brandefelt J., Kjellström E., Smith B., 2011. High resolution simulation of last  
1256 glacial maximum climate in Europe. Tellus 63 A, 107-125.  
1257

1258 Sun, J., Muhs, D.R., 2007. Dune Fields | Mid-Latitudes, in: Elias, S.A. (Ed.), Encyclopedia of  
1259 Quaternary Science. Elsevier, Oxford, pp. 607–626.  
1260

1261 Taylor, S.R., McLennan, S.M., 1995. The geochemical evolution of the continental crust.  
1262 Reviews of Geophysics 33, 241-265.  
1263

1264 Thibault, C., 1970. Recherches sur les terrains quaternaires du bassin de l'Adour. Thèse  
1265 d'état, Université de Bordeaux, Bordeaux, 814 pp.  
1266

1267 Tsoar, H., 1978. The Dynamics of Longitudinal Dunes. (Final technical report). DTIC  
1268 Document, London: European Research Office, US Army, 171 pp.  
1269

1270 Tsoar, H., Pye, K., 1987. Dust transport and the question of desert loess formation.  
1271 Sedimentology 34, 139–153.  
1272

1273 Van Huissteden, Ko (J), Schwan, J.C.G., Bateman, M.D., 2001. Environmental conditions  
1274 and paleowind directions at the end of the Weichselian Late Pleniglacial recorded in aeolian  
1275 sediments and geomorphology (Twente, Eastern Netherlands). Geologie en Mijnbouw /  
1276 Netherlands Journal of Geosciences 80, 1–18.  
1277

1278 van Huissteden, K., Pollard, D., 2003. Oxygen isotope stage 3 fluvial and eolian successions  
1279 in Europe compared with climate model results. Quaternary Research 59, 223–233.  
1280

1281 van Meerbeeck, C.J., Renssen, H., Roche, D.M., 2009. How did Marine Isotope Stage 3 and  
1282 Last Glacial Maximum climates differ? – Perspectives from equilibrium simulations. Climate  
1283 of the Past 5, 33-51.  
1284

1285 Waggoner P.E., Bingham C., 1961. Depth of loess and distance from source. *Soil Science* 92,  
1286 396–401.  
1287

1288 Warren, A., 1972. Observations on Dunes and Bi-Modal Sands in the Ténéré Desert.  
1289 *Sedimentology* 19, 37–44.  
1290

1291 Webster, R., Oliver, M.A., 2007. *Geostatistics for environmental scientists. Statistics in*  
1292 *practice.* Wiley, Chichester, 315 pp.  
1293

1294 Wedepohl, K.H., 1978. *Handbook of geochemistry.* Springer-Verlag, Berlin, Heidelberg, 443  
1295 pp.  
1296

1297 Wiggs, G., Bullard, J., Garvey, B., Castro, I., 2002. Interactions Between Airflow and Valley  
1298 Topography with Implications for Aeolian Sediment Transport. *Physical Geography* 23, 366–  
1299 380.  
1300

1301 Wojdyr M. J., 2010 : *Fityk*: a general-purpose peak fitting program. *Journal of Applied*  
1302 *Crystallography*, 43, p. 1126-1128.  
1303

1304 Wolfe, S., 2004. Relict Late Wisconsinan Dune Fields of the Northern Great Plains, Canada.  
1305 *Géographie physique et Quaternaire* 58, 323–336.  
1306

1307 Wolfe, S.A., Moorman, B.J., Hugenholtz, C.H., 2008. Effects of sand supply on the  
1308 morphodynamics and stratigraphy of active parabolic dunes, Bigstick Sand Hills,  
1309 southwestern Saskatchewan. *Canadian Journal of Earth Sciences* 45, 321–335.  
1310

1311 Wright, J., Smith, B., Whalley, B., 1998. Mechanisms of loess-sized quartz silt production  
1312 and their relative effectiveness: laboratory simulations. *Geomorphology* 23, 15–34.  
1313

1314 Wu, H., Guiot, J., Brewer, S., Guo, Z., 2007. Climatic changes in Eurasia and Africa at the  
1315 last glacial maximum and mid-Holocene: reconstruction from pollen data using inverse  
1316 vegetation modelling. *Climate Dynamics* 29, 211–229.  
1317



1318 Zeeberg, J., 1998. The European sand belt in Eastern Europe - and comparison of Late Glacial  
1319 dune orientation with GCM simulation results. *Boreas* 27, 127–139.

1320

## 1321 **Figures**

1322 Fig. 1: European aeolian deposits. A – General map from Bertran et al. (2016) and location of  
1323 the study area; B – Close-up view of southwest France. The distribution of ventifacts is from  
1324 Bertran et al. (2011).

1325

1326 Fig. 2: Modern meteorological parameters in the studied area. A - Roses of seasonal winds in  
1327 Aquitaine (period 1999-2007) according to MétéoFrance (Ile d'Yeu weather station); B -  
1328 Mean wind speeds ( $m.s^{-1}$ ) at a height of 80 m, from Agri4cast (2016); the dashed line  
1329 indicates the coversand limit.

1330

1331 Fig. 3: A, B - Detailed topography of barchanoid ridges (photogrammetry); location shown in  
1332 Figure 4A. pr – Pleistocene ridge field; hs: Holocene sand cover at the front of a parabolic  
1333 dune. North to the top. A', B' – Aerial views of the same areas ( photos IGN / Google Earth).

1334

1335 Fig. 4: View of transverse ridges dated to MIS 2, Pontonx-sur-l'Adour.

1336

1337 Fig. 5: Ridges of the Plateau Girondin. A – Distribution of low-amplitude ridges (zibars) and  
1338 orientation of the vector perpendicular to dune crests. B – Topographic transect between the  
1339 Atlantic coast and the Garonne river, and associated dunes morphologies. C – Photo-mosaic  
1340 of fields showing low-amplitude ridges (photos IGN / Google Earth) with superimposed 5 m  
1341 contour lines, and close-up view of ridge fields.

1342

1343 Fig. 6: Distribution of parabolic dunes (in red) according to the 1:50,000 geologic map  
1344 (Bureau des Recherches Géologiques et Minières) and orientation of the bisector of the angle  
1345 between the two arms for simple and complex dunes. The rectangles indicate the location of  
1346 figures 6A-D.

1347

1348 Fig. 7: Parabolic dunes, 5 m DEM (RGE Alti® 2.0, IGN 2014). The areas represented are  
1349 shown in Figure 5. A – Dunes (indicated by white arrows) on both left and right banks of a  
1350 river; B – Compound elongated parabolic dune; C - Parabolic dunes on the right (i.e. wind-  
1351 facing) bank of a river; D - Dunes on the left bank of a river.

1352

1353 Fig. 8: Grain-size maps of the aeolian deposits interpolated by ordinary kriging. The white  
1354 dots correspond to the sites used for kriging. The dotted line indicates the coversand limit.

1355

1356 Fig. 9: Detailed maps of the coarse (upper panel) and fine (bottom panel) silt content in the  
1357 northern (A) and the southern (B) part of the Aquitaine basin.

1358

1359 Fig. 10: Evolution of the grain-size mode of some representative samples from the southern  
1360 part of the basin. The modes were established after deconvolution of the grain-size curves  
1361 using the software Fityk 0.9.8 (Wojdyr, 2010). The location of the samples is shown in  
1362 Figure 8.

1363

1364 Fig. 11: Grain size distribution of some representative samples of sandy silts and loess from  
1365 the Landes district. The location of the samples is shown in Figure 8.

1366

1367 Fig. 12: Map of the thickness of the loess located on the right bank of the Garonne river (A)  
1368 and on the left bank of the Adour river (B). The coversand limit is indicated by a dashed line.

1369

1370 Fig. 13: Maps of the content in some elements of the aeolian and alluvial deposits. Fines = silt  
1371 + clay.

1372

1373 Fig. 14: Ti, Zr, K and Al – Si scattergrams of aeolian and alluvial samples of the Aquitaine  
1374 basin. UCC: upper continental crust composition according to Taylor and McLennan (1995).  
1375 a – adjustment line for loess and the alluvial deposits of the Leyre and Ciron rivers; b –  
1376 adjustment line for other alluvial deposits.

1377

1378 Fig. 15: Principal component analysis adapted to compositional data (“compositional biplot”)  
1379 of major and minor elements (fraction > 63  $\mu\text{m}$ ) of aeolian and potential source deposits.

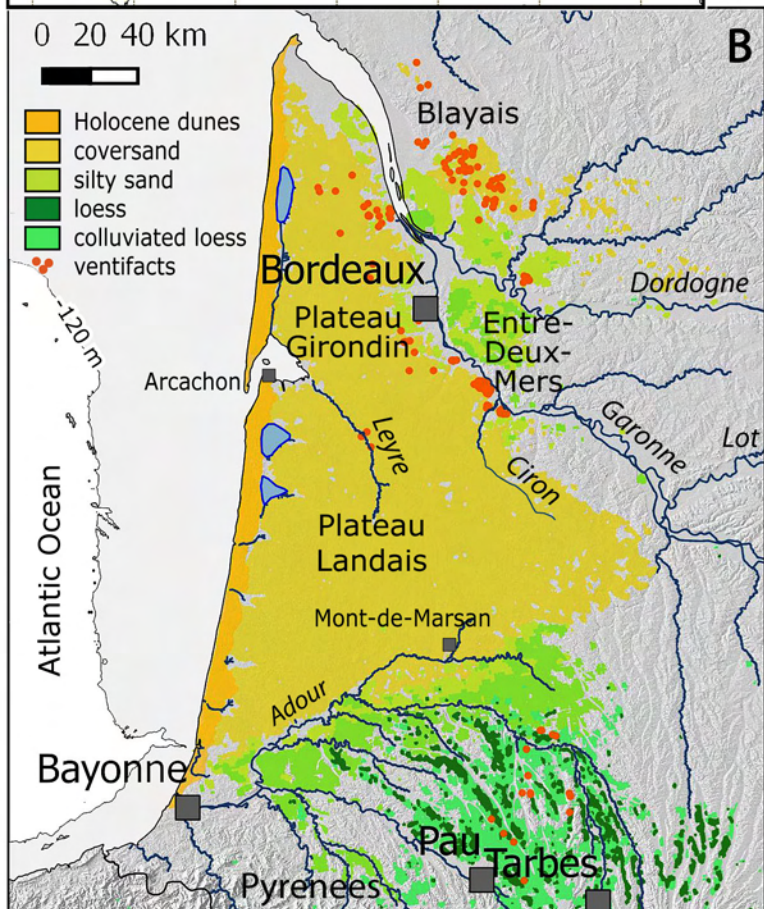
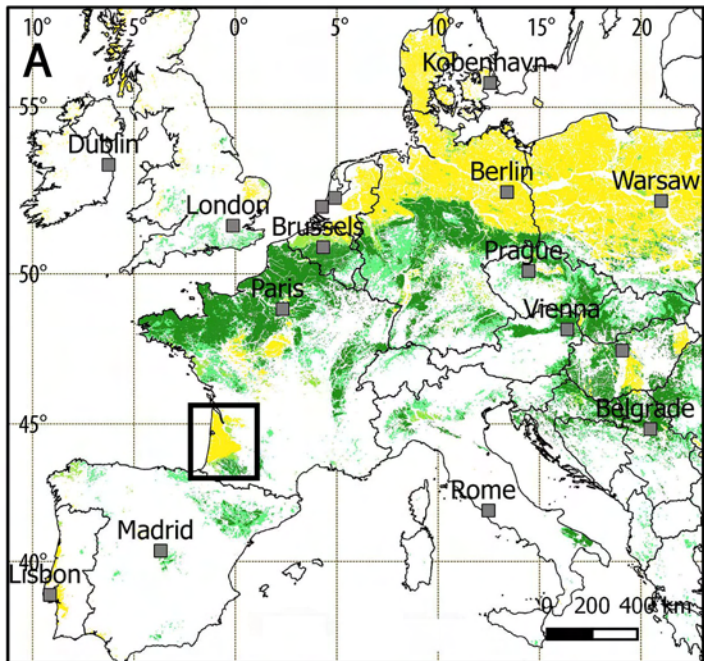
1380

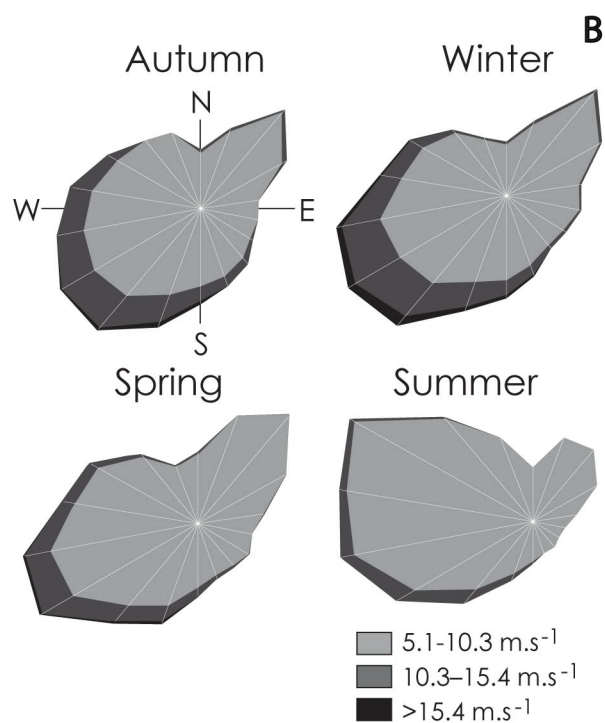
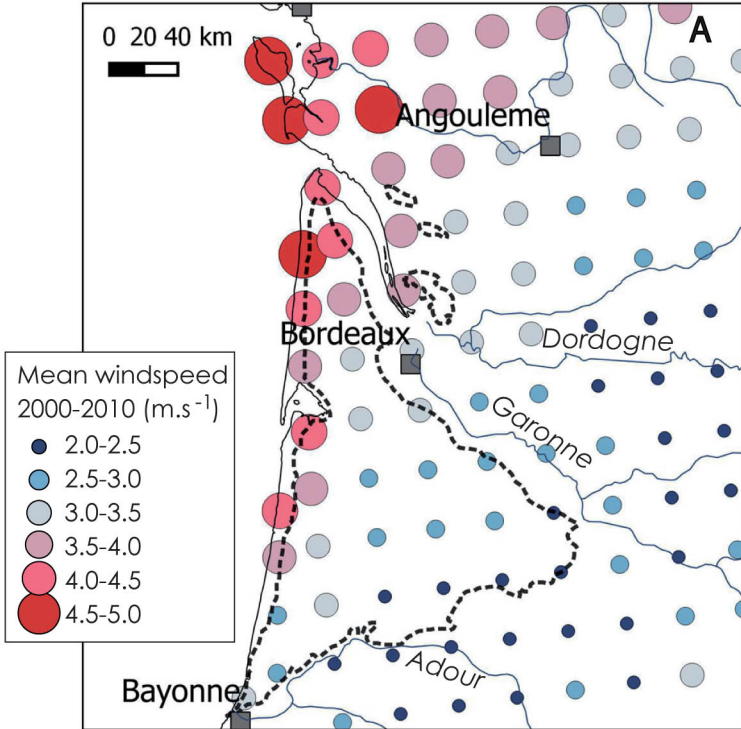
1381 Fig. 16: Compositional biplot of major and minor elements (fraction < 63  $\mu\text{m}$ ) of aeolian and  
1382 potential sources deposits.

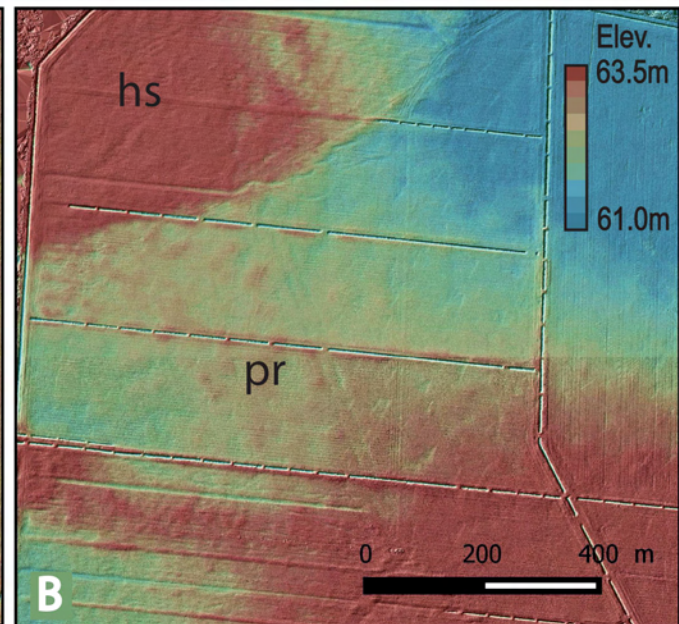
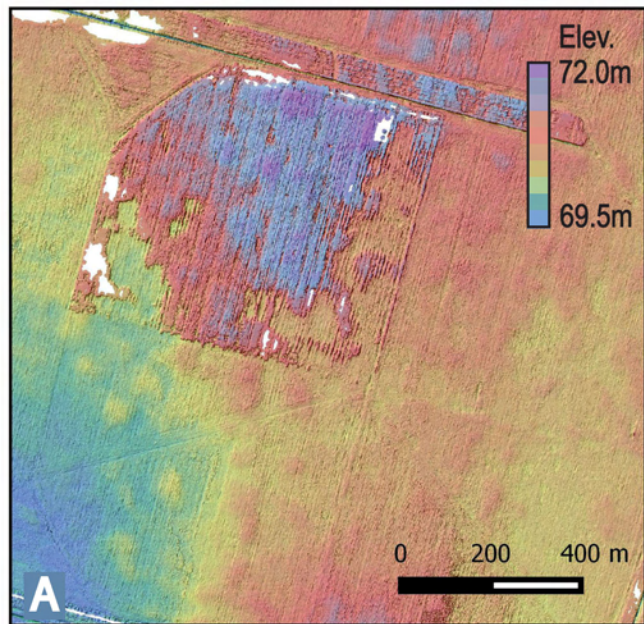
1383

1384 Fig.17: Annual cycle of surface winds and ground conditions for the LGM and MIS 3  
1385 simulations (averaged over the domain between longitude 2°W-1°E and latitude 43°-45.5°N,

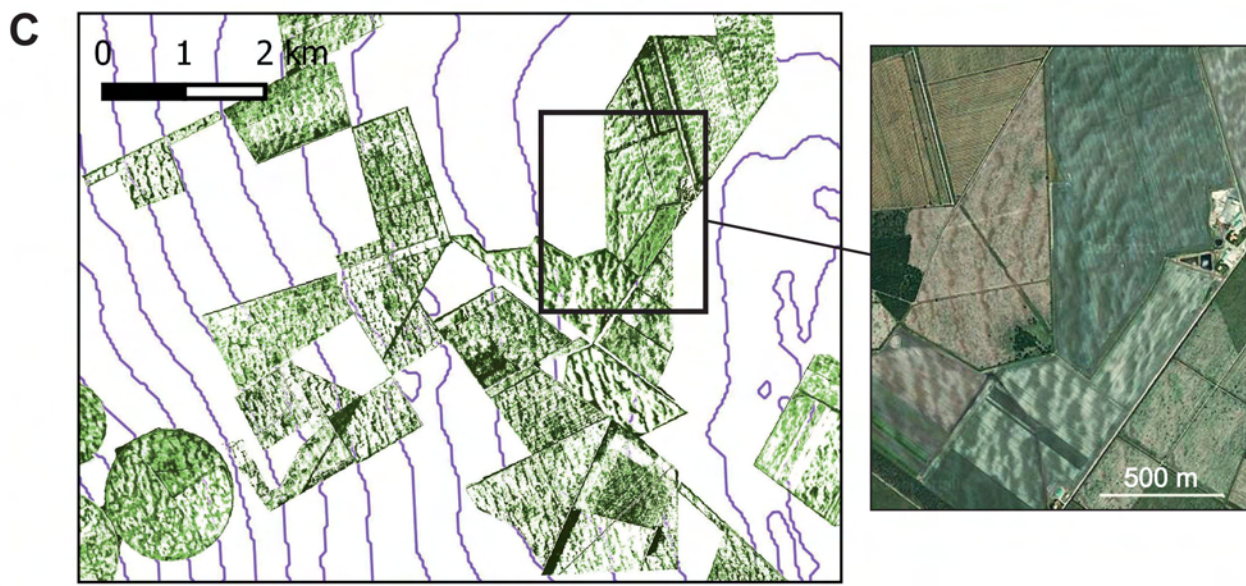
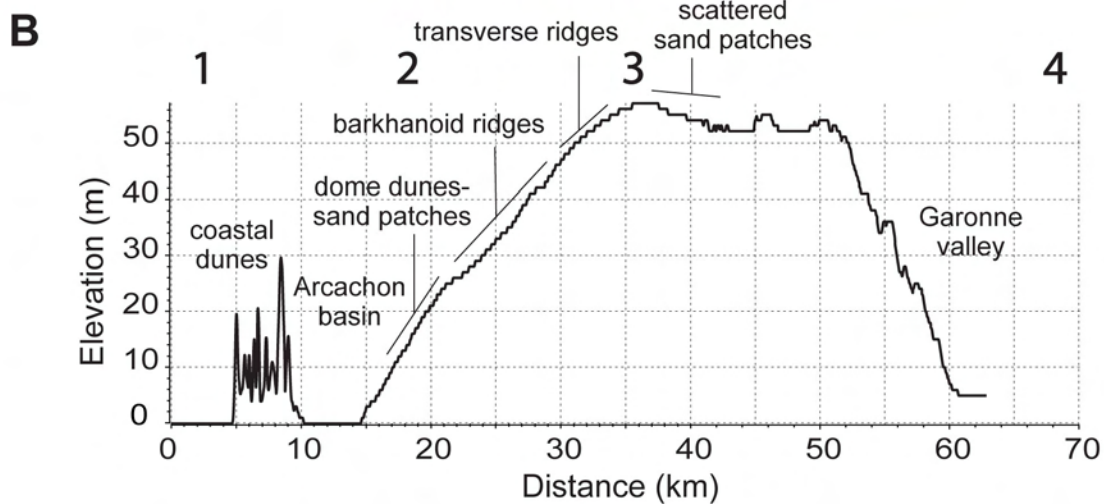
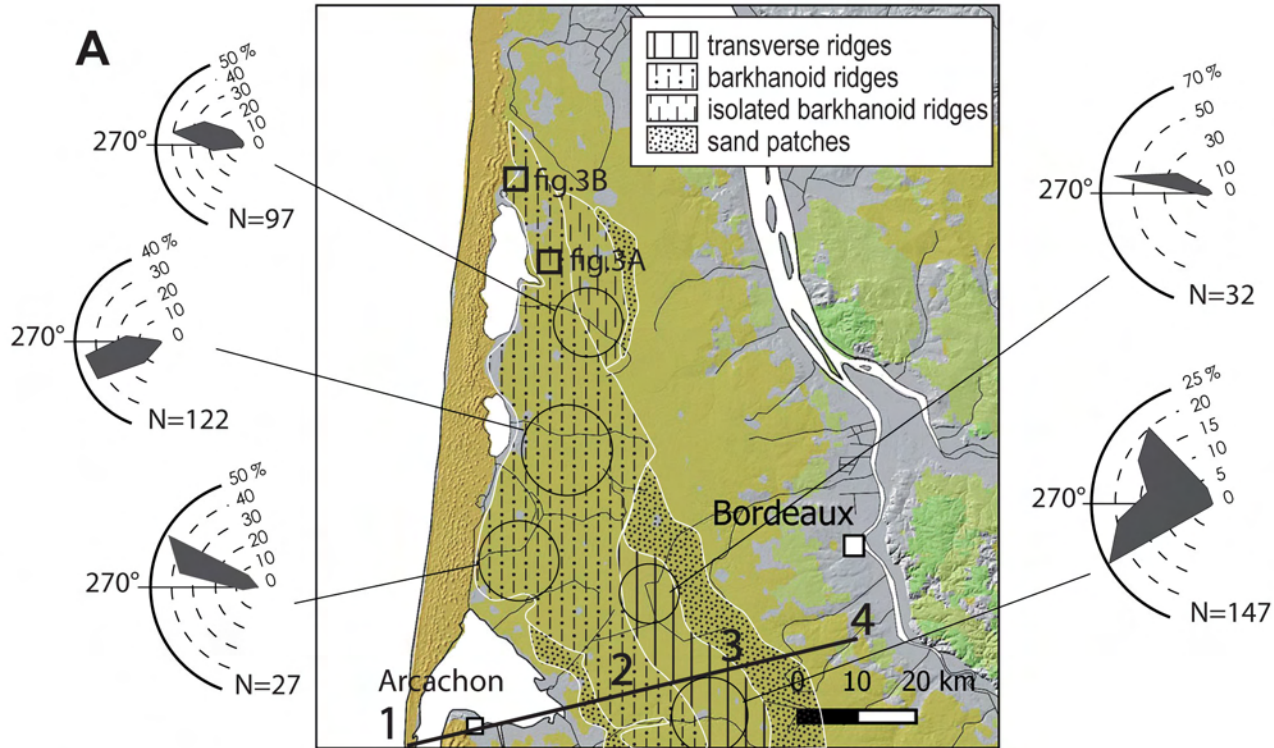
1386 and over 20 years for each run). From top to bottom: wind direction, daily maximum wind  
1387 speed for different values of roughness length ( $z_0$ ), and ground conditions (dry soil depth and  
1388 percent of snow-free surface). Red dashed lines mark the different thresholds discussed in the  
1389 text. Red rectangles indicate the most probable period of deflation according to the available  
1390 constraints.



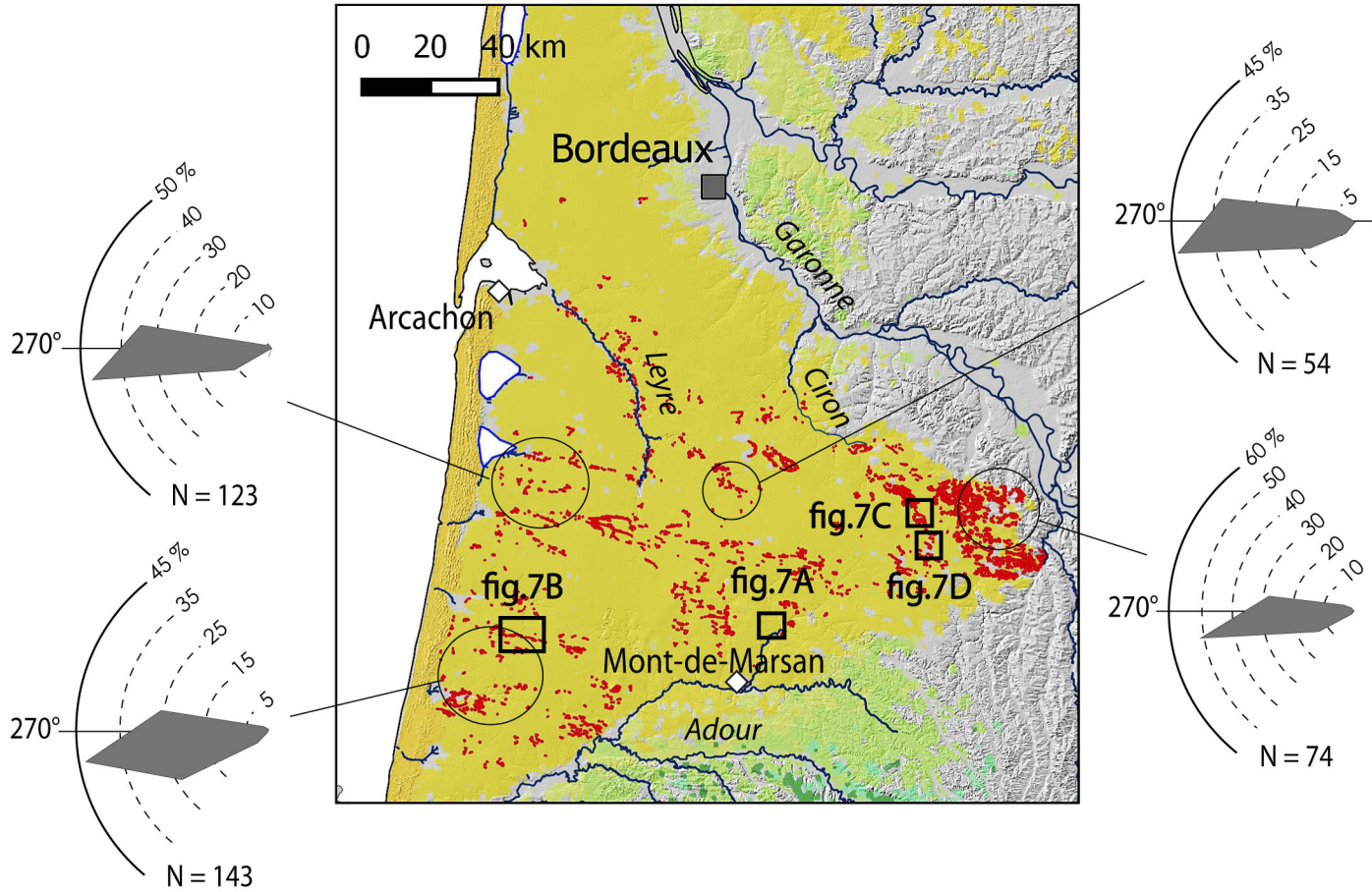


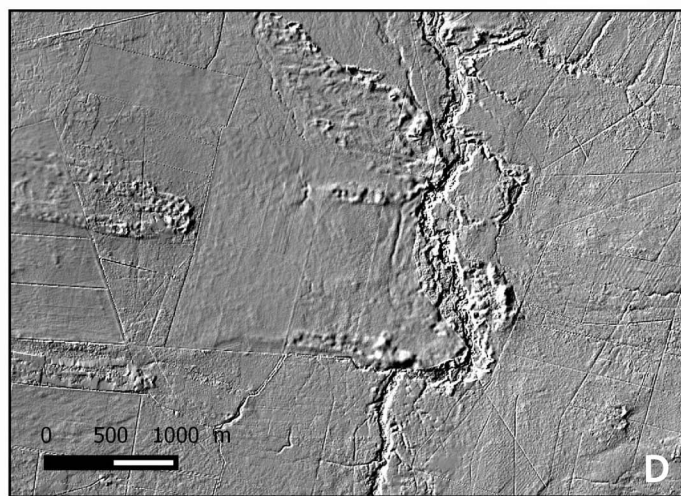
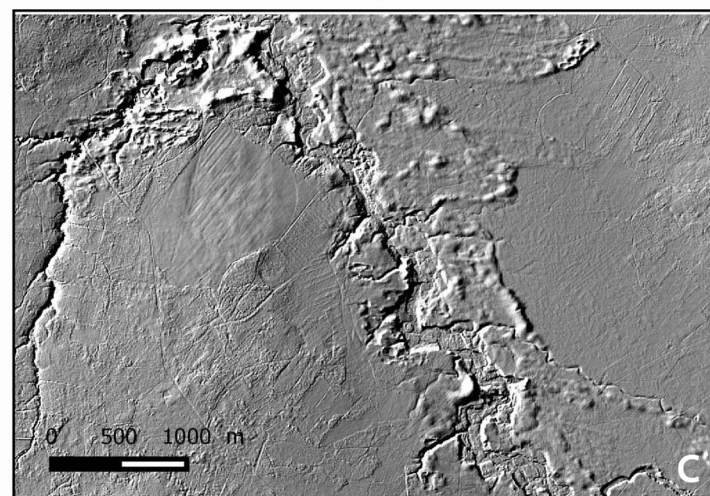
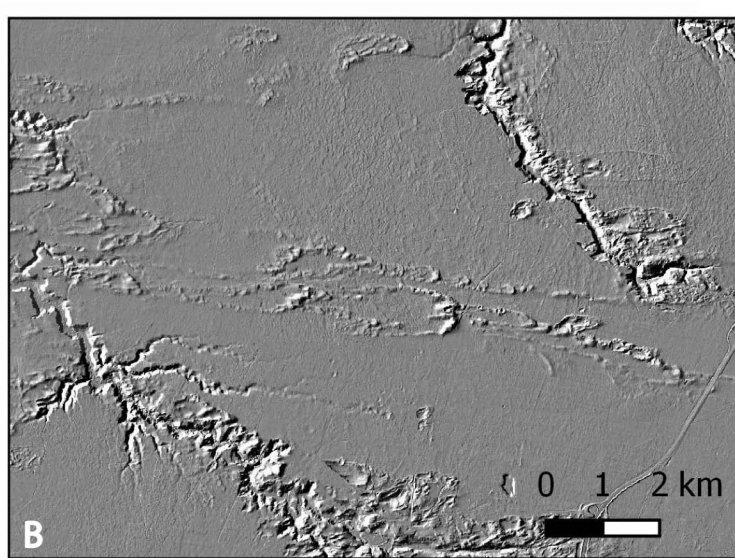
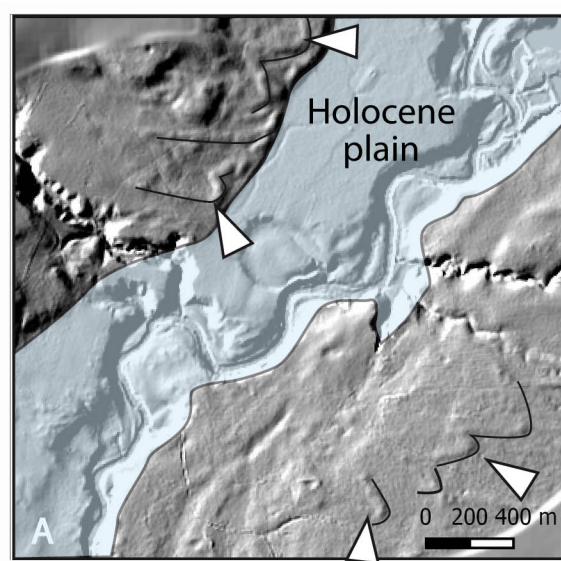




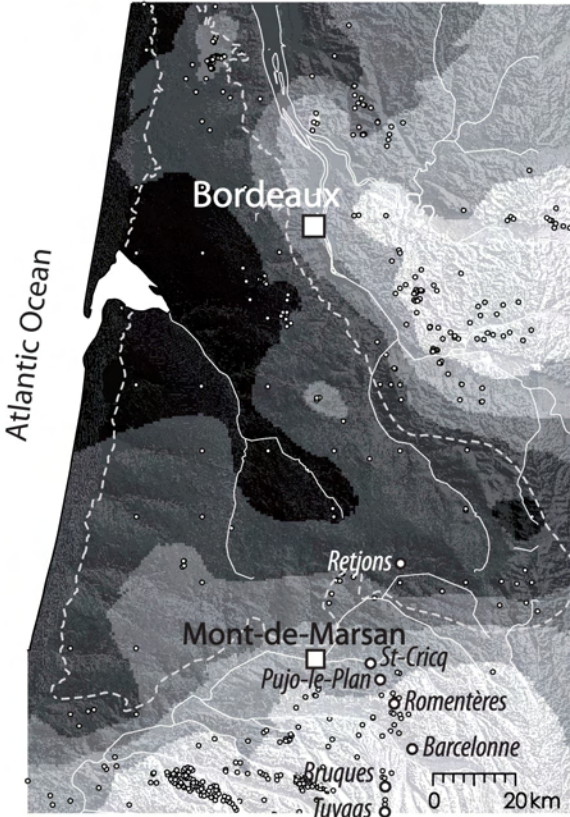
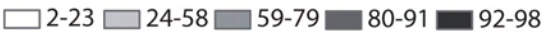




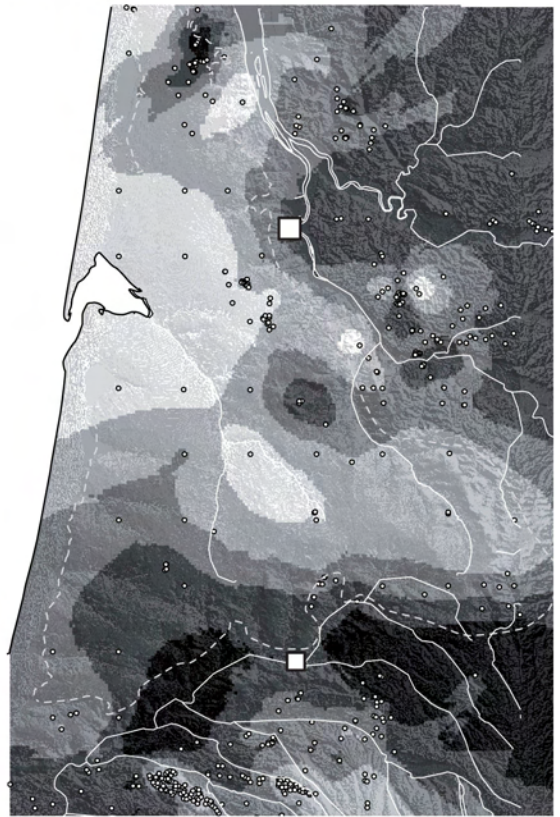




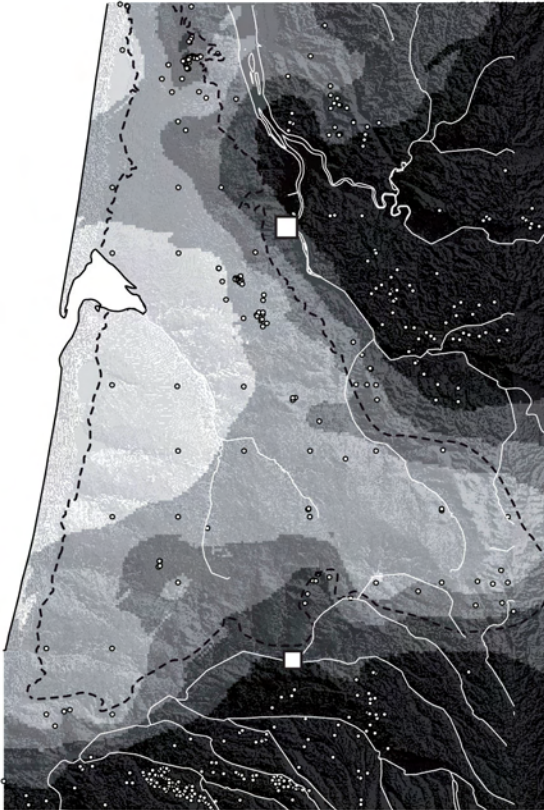
Medium to coarse sand (2000 - 200  $\mu\text{m}$ ) %



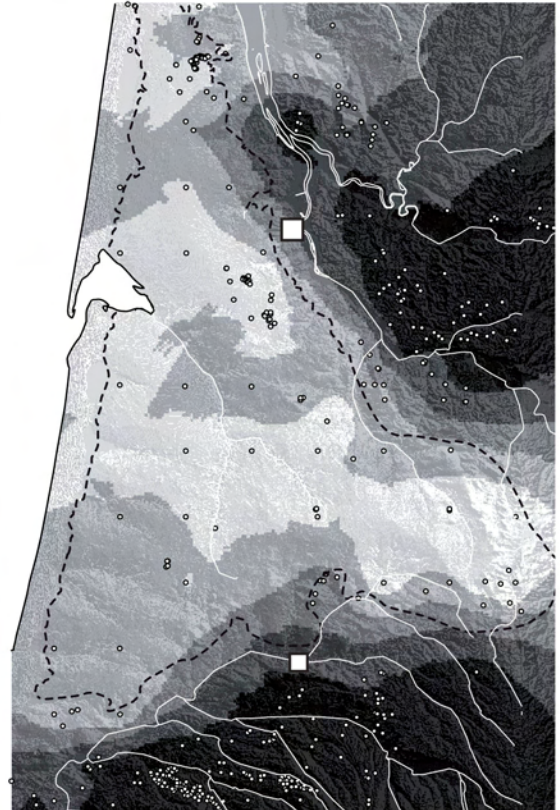
Fine sand (200 - 50  $\mu\text{m}$ ) %



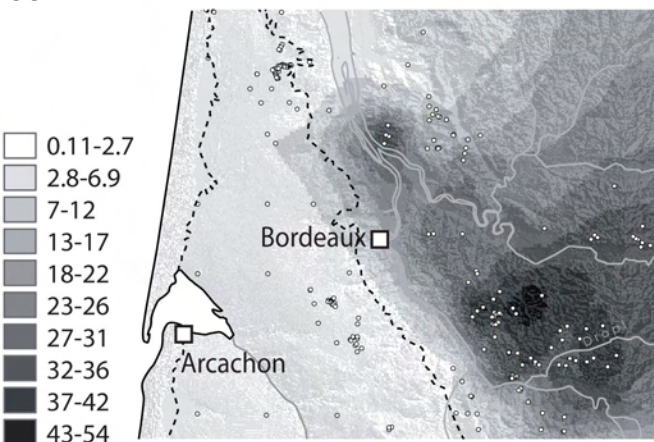
Coarse silt (50 - 20  $\mu\text{m}$ ) %



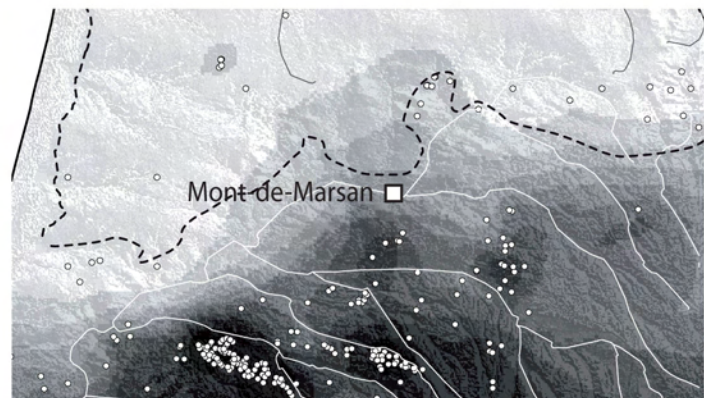
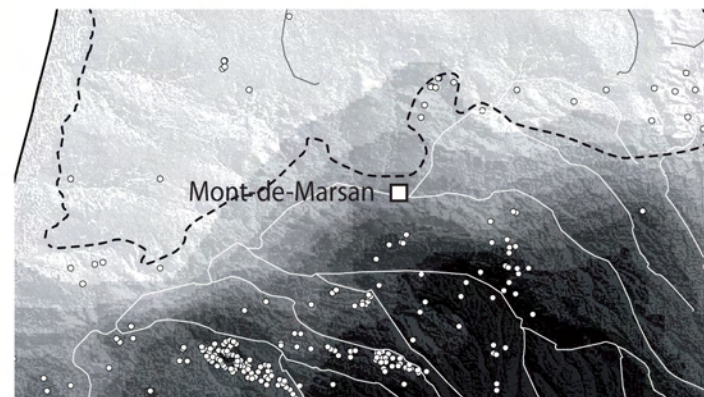
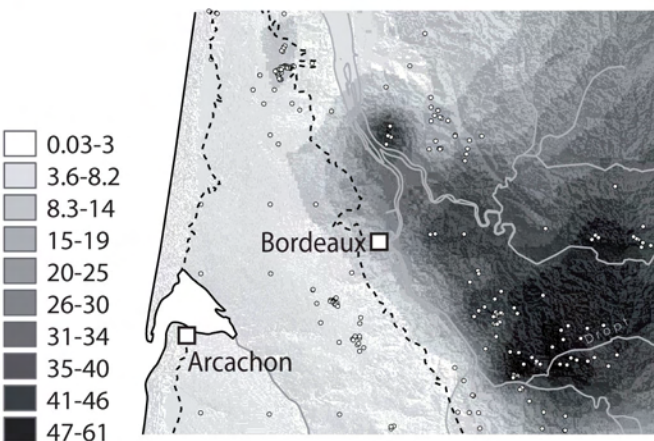
Fine silt (20 - 2  $\mu\text{m}$ ) %



A



B

Coarse silt (50 - 20  $\mu\text{m}$ ) %Fine silt (20 - 2  $\mu\text{m}$ ) %

0 16 km

